https://doi.org/10.11820/xxxxxxxxxxxxx_0002

Chapter 2

Magnonics and Confinement of Light in Photonic–Magnonic Crystals

Jarosław W. Kłos[*,**], Igor L. Lyubchanskii[†,‡], Maciej Krawczyk[*], Paweł Gruszecki[*], Szymon Mieszczak[*], Justyna Rychły[*,§], Yuliya S. Dadoenkova[¶,‖], and Nataliya N. Dadoenkova[‖]

[*] *Faculty of Physics, Adam Mickiewicz University Uniwersytetu Poznańskiego 2, 61-614 Poznań, Poland*
[†] *Donetsk Institute for Physics and Engineering named after O. O. Galkin (branch in Kharkiv) of the National Academy of Sciences of Ukraine, 03028 Kyiv, Ukraine*
[‡] *V. N. Karazin Kharkiv National University, 61022 Kharkiv, Ukraine*
[§] *Institute of Molecular Physics, Polish Academy of Sciences, Mariana Smoluchowskiego 17, 60-179 Poznań, Poland*
[¶] *Lab-STICC (UMR 6285), CNRS, ENIB, 29238 Brest Cedex 3, France*
[‖] *Ulyanovsk State University, 432017 Ulyanovsk, Russia*

We discuss the spin-wave confinement in the magnetic components of magnetophotonic structures. In the initial sections of the chapter, we describe the principles of magnetization dynamics, including both the exchange and dipolar interactions. We showed that the spin-wave spectrum in confined geometry is determined not only by the spatial constraints but is also strongly influenced by non-local demagnetizing effects. In addition, we analyze the localization of light in the regions of spin-wave confinement, which can strengthen the magneto–optical interaction. Such enhancement can be potentially realized in photonic–magnonic crystals, where

[**]Corresponding author: klos@amu.edu.pl

the light localization in magnetic components of the structure results from the periodicity and the spin waves co-exist with electromagnetic waves. The final sections are devoted to the Faraday effect and Goos–Hänchen effect in photonic–magnonic crystals.

1. Introduction

Magnetic moments can rotate in the precessional motion around the direction of the static magnetic field if they are pushed out of the equilibrium orientation (e.g., by the application of a radio frequency electromagnetic field). Due to the interactions in a magnetic medium, the waves of coherently precessing magnetic moments can propagate over large distances, as compared to their wavelength. These waves (called spin waves[1–4]) can transmit energy and information, similarly, like other kinds of waves (e.g., electromagnetic waves[5]). Typical frequencies of spin waves (in the range from a fraction of GHz to hundreds of GHz) and their wavelengths (in the range from hundreds to tens of nanometers, respectively) make possible the design of miniaturized devices (called magnonic devices) operating on high-frequency signals at nanometer scale.[6,7]

The spin waves are confined in the volume of the magnetic body. The static magnetic configuration and the dynamics of magnetic moments are governed by the magnetic interactions which act both in long- and short-range. Due to the long-range character of magnetic interactions, the magnetization dynamics depends on the geometry of the system. The confinement of spin waves in magnetic structures results not only in the quantization of the waves in constrained dimensions but also determines the dipolar interactions.[8,9]

The frequencies of spin waves correspond to the frequencies of microwaves. Therefore the direct coupling between spin waves and electromagnetic waves (microwaves) is possible. It is also feasible to observe the inelastic scattering of light of optical frequency on the spin waves in the process called Brillouin light scattering (BLS).[10] The high frequencies of optical electromagnetic waves also allow for scoping static magnetic configuration and the dynamics of magnetization by Kerr or Faraday[11] effect where the (temporal) changes of polarization of the reflected or transmitted light give the information about the statics (dynamics) of magnetization.[12]

For all of these effects, the interaction between spin waves and electromagnetic waves strongly depends on the localization of both kinds of waves. The interaction can be significantly enhanced when the spin waves and electromagnetic waves are spatially confined in the same area.

To effectively mold the propagation and localization of spin waves or electromagnetic waves, we can use the artificial periodic structures called magnonic crystals[6,13] and photonic crystals,[14] respectively. The spectra of wave eigenmodes in these structures are split into the frequency ranges forbidden (frequency band gaps) and allowed for propagating waves (frequency bands). The photonic crystals containing magnetic materials (magnetophotonic crystals) are the subject of intensive studies[15–17] because they allow exploring the chiral magneto–optical effects for electromagnetic waves. However, they are not structurally optimized to support the existence of spin waves. In order to play with the interaction of spin waves and electromagnetic waves in periodic structures, we need the particular kind of artificial crystal, named as photonic–magnonic crystal.[18–20] In photonic–magnonic crystals, we use the photonic band gaps to localize the electromagnetic waves in periodically placed magnetic layers, playing the role of artificial defects. In such conditions, both the magneto–optical effects (as it was shown for BLS, Faraday[21] and Goos–Hänchen[22] effects) and the interaction (between localized spin waves and electromagnetic waves) can be strengthened.[23–25]

1.1. *Landau–Lifshitz equation*

The dynamics of the magnetic moment $\mathcal{M}(t)$ can be classically described by Landau–Lifshitz equation[1,26,27]:

$$\frac{d\mathcal{M}(t)}{dt} = \gamma\mu_0\mathcal{M}(t) \times \mathbf{H}_{\text{eff}}(t), \tag{1}$$

where $\mathbf{H}_{\text{eff}}$ is an effective field. The effective field includes both the external field $\mathbf{H}_0$, produced by electric currents, and the internal field $\mathbf{H}_{\text{int}}$, resulting from the interactions with the other magnetic moments. The coefficient γ is called gyro-magnetic ratio and relates the magnetic moments to the angular momentum: $\gamma = \mathcal{M}/\mathbf{J}$.

For negatively charged particles (e.g., for electron) the angular momentum (spin) is oriented in opposite direction to magnetic moment and therefore their gyro-magnetic ratio is negative. Equation (1) can be classically derived from the equation of motion for angular momentum:

$$\frac{d\mathbf{J}}{dt} = \mathcal{T}, \tag{2}$$

where the torque $\mathcal{T}$ has magnetic origin: $\mathcal{T} = \mathcal{M} \times \mathbf{B}_{\text{eff}} = \mu_0 \mathcal{M} \times \mathbf{H}_{\text{eff}}$. The Landau–Lifshitz equation (1) describes dynamics which conserves the length of the magnetic moment vector. It can be easily noticed after calculations of scalar product of both sides of the equation (1) with $\mathcal{M}(t)$ which gives the relation: $\partial|\mathcal{M}(t)|^2/\partial t = 0 \implies |\mathcal{M}(t)|$=const.

For continuous medium the equation can be written in the local form, where the magnetization vector $\mathbf{M}$, as a magnetic moment $\mathcal{M}$ per unit of volume v ($\mathbf{M} = d\mathcal{M}/dv$), is introduced:

$$\frac{\partial \mathbf{M}(\mathbf{r},t)}{\partial t} = \gamma(\mathbf{r}) \underbrace{\mu_0 \mathbf{M}(\mathbf{r},t) \times \mathbf{H}_{\text{eff}}(\mathbf{r},t)}_{\mathbf{T}(\mathbf{r},t)}, \tag{3}$$

where $\mathbf{T}$ is a torque per unite volume of the magnetic material. The internal components of effective field are determined by the spatial distribution and temporal changes of magnetization vector: $\mathbf{H}_{\text{int}}(\mathbf{r},t) = \mathbf{H}_{\text{int}}(\mathbf{M}(\mathbf{r},t))$. This feature makes Eq. (3) nonlinear in the general case. Therefore, the Landau–Lifshitz equation describes the variety of dynamical effect including both the nonlinear and linear phenomena, e.g., magnetization switching, domain wall motion, and dynamics, vortex dynamics and spin-wave propagation.

The magnetization in the solids results primarily from the presence of magnetic moments of electronic spins. Therefore in further consideration we assume that $\gamma(\mathbf{r}) < 0$.

1.2. *Linear approximation*

Let us consider the magnetization vector oriented at the oblique direction in an effective magnetic field. According to Eq. (3), the

torque $\mathbf{T} = \mu_0 \mathbf{M} \times \mathbf{H}_{\text{eff}}$ is orthogonal to the direction of magnetization and to the direction of effective field. When the effective field is static, then the magnetization precesses around the direction of the effective field $\hat{\mathbf{n}}$, as it is shown in Fig. 1. (It is worth noting that for

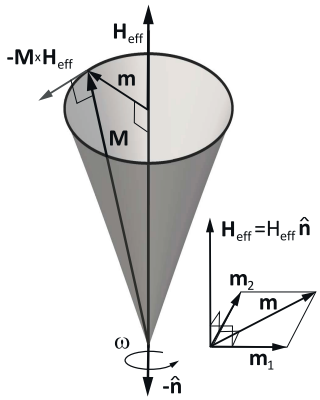

Fig. 1. The precession of magnetization vector around the static component of the effective field for $\gamma < 0$. The dynamic magnetization $\mathbf{m}$ can be presented as a sum of two orthogonal components: $\mathbf{m}_1$ and $\mathbf{m}_2$. The torque: $\mathbf{T} = \mu_0 (\mathbf{M} \times \mathbf{H}_{\text{eff}})$ keeps the head of magnetization vector on elliptical path in the absence of dumping.

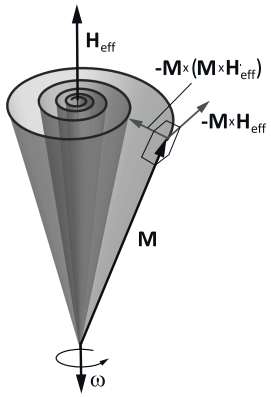

Fig. 2. The precession of magnetization vector around the direction of the effective field in the presence of Landau damping. The damping torque: $\mathbf{T}_d = \lambda \frac{\mu_0}{M_s} \mathbf{M} \times (\mathbf{M} \times \mathbf{H}_{\text{eff}})$ aligns gradually the magnetization vector to the direction of effective field. Similarly like in Fig. 1, we presented the case for $\gamma < 0$.

$\gamma < 0$ the direction of precession is the same as the direction of the effective field: $\boldsymbol{\omega} = \omega\hat{\mathbf{n}}$).

When the angle of the precession cone is small, then Eq. (3) can be linearized. Firstly, we are justified to assume that the component of magnetization along the direction of the effective field is static and its length is approximately equal to the saturation magnetization M_S. Then, we can consider the component of magnetization orthogonal to the effective field as a small and oscillating harmonically in time:

$$\mathbf{M}(\mathbf{r}, t) = M_{\mathrm{S}}(\mathbf{r})\hat{\mathbf{n}}(\mathbf{r}) + \mathbf{m}(\mathbf{r})e^{i\omega t}, \tag{4}$$

where $\mathbf{m} \cdot \hat{\mathbf{n}} = 0$. The unit vector $\hat{\mathbf{n}}(\mathbf{r})$ describes the static magnetic configuration which is not co-linear in general. The positive value of ω in the exponent $e^{i\omega t}$ corresponds to the negative value of γ. The vector $\mathbf{m}$ (of small magnitude $|m| \ll M_{\mathrm{S}}$) can be expressed by two orthogonal complex components: m_1 and m_2. The difference between the arguments of m_1 and m_2 is a phase difference between the oscillation of magnetization in two orthogonal direction during the precessional motion (e.g., for fully circular precession $|\mathrm{Arg}(m_1) - \mathrm{Arg}(m_2)| = \pi/2$). The same shift of the arguments for both components ($m_1 \to m_1 e^{i\varphi_0}$, $m_2 \to m_2 e^{i\varphi_0}$) is irrelevant from physical point of view and can be interpreted as selection of a initial time for the observation of precessional motion: $\phi_0 = \varphi_0/\omega$. The effective field can be represented similarly by splitting into the static part and small dynamic part, which oscillates harmonically in time

$$\mathbf{H}_{\mathrm{eff}}(\mathbf{r}, t) = H_{\mathrm{eff}}(\mathbf{r})\hat{\mathbf{n}}(\mathbf{r}) + \mathbf{h}(\mathbf{r})e^{i\omega t}. \tag{5}$$

We limited our considerations to the case when the external field has only static component $\mathbf{H}_0$ and does not contribute to the dynamic part of effective field. The dynamic field $\mathbf{h}(\mathbf{r})e^{i\omega t}$ results only from dynamic interactions within the magnetic system and is (mutually) related only to the spatial distribution of dynamic component of magnetization $\mathbf{m}(\mathbf{r})$. It means that $\mathbf{h}$ is not able to change the static configuration $\hat{\mathbf{n}}(\mathbf{r})$.

Taking into account the assumptions discussed above, we can obtain the following form of linearized Landau–Lifshitz equation for

$\gamma < 0$:

$$i\omega \mathbf{m}(\mathbf{r}) = |\gamma| \mu_0 \left(H_{\text{eff}}(\mathbf{r}) \mathbf{m}(\mathbf{r}) - M_{\text{S}}(\mathbf{r}) \mathbf{h}(\mathbf{r}) \right) \times \hat{\mathbf{n}}(\mathbf{r}), \tag{6}$$

where we neglected the weak spatial dependence of $\gamma(\mathbf{r})$. In Eq. (6), we omitted the product: $\mathbf{h}(\mathbf{r}) e^{i\omega t} \times \mathbf{m}(\mathbf{r}) e^{i\omega t} \propto e^{i2\omega t}$ which is nonlinear.

The linearized spin-wave dynamics has a form of precessional motion of magnetization vector around the direction of the effective field where only the harmonic dynamics in the direction perpendicular to a static effective field is considered. Equation (6) allows to find the spatial distribution of the complex amplitude $\mathbf{m}(\mathbf{r})$ of dynamical comment of magnetization at a given frequency ω.

It is worth noting that the reverse of direction of static effective field: $\hat{\mathbf{n}} \to -\hat{\mathbf{n}}$ leads to the reversal of the precession direction: $\omega \to -\omega$ for the same spatial distribution of the dynamic magnetization $\mathbf{m}(\mathbf{r})$.

1.3. *Magnetic damping*

The energy of spin waves is dissipated directly or indirectly to the lattice vibrations (heat) or, in a smaller extent, to the electromagnetic radiation. Regardless of the microscopic mechanism, the spin-wave damping can be described by the introduction of additional torque $\mathbf{T}_d$ (see Fig. 2) to the Landau–Lifshitz equation which drags the magnetization vector towards the direction of the effective field. One possible formulation of the damping term was proposed by Landau:

$$\frac{\partial \mathbf{M}}{\partial t} = \gamma \underbrace{\mu_0 (\mathbf{M} \times \mathbf{H}_{\text{eff}})}_{\mathbf{T}} + \gamma \underbrace{\frac{\lambda}{M_{\text{S}}} \left(\mathbf{M} \times \overbrace{\mu_0 (\mathbf{M} \times \mathbf{H}_{\text{eff}})}^{\mathbf{T}} \right)}_{\mathbf{T}_{d,L}}. \tag{7}$$

The alternative form of damping torque was formulated by Gilbert[28]:

$$\frac{\partial \mathbf{M}}{\partial t} = \gamma \underbrace{\mu_0 (\mathbf{M} \times \mathbf{H}_{\text{eff}})}_{\mathbf{T}} + \gamma \underbrace{\frac{\alpha}{M_{\text{S}}} \left(\mathbf{M} \times \frac{1}{\gamma} \frac{\partial \mathbf{M}}{\partial t} \right)}_{\mathbf{T}_{d,G}}. \tag{8}$$

The dimensionless parameters λ and α denote the strength of the torque's damping for Landau formulation ($\mathbf{T}_d = \mathbf{T}_{d,L}$) or Gilbert ($\mathbf{T}_d = \mathbf{T}_{d,G}$). For small damping ($\mathbf{T}_d \ll \mathbf{T}$) the difference: $\frac{1}{\gamma}\frac{\partial \mathbf{M}}{\partial t} - \mathbf{T}$ is small and both formulations of damping torques are practically equivalent. In the regime of small damping the parameters α and λ take practically the same values. For large damping both descriptions are not equivalent. The formulation of damping torque proposed by Gilbert agrees better with experimental results. In order to force the Landau formulation to be exactly equivalent to those proposed by Gilbert we have to replace λ by $\alpha/(1+\alpha^2)$ and renormalize the gyromagnetic factor: $\gamma \to \gamma_G = \gamma/(1+\alpha^2)$. For both formulations of damping torque, the length of magnetization vector $|\mathbf{M}(t)|$ is conserved.

The linearized versions of Eqs.(7) and (8) can be written in the following forms for $\gamma < 0$:

$$i\omega \mathbf{m} = |\gamma|\mu_0 \left[H_{\text{eff}} \left(\mathbf{m} \times \hat{\mathbf{n}} + \lambda \mathbf{m}\right) - M_{\text{S}} \left(\mathbf{h} \times \hat{\mathbf{n}} + \lambda \mathbf{h}\right)\right] \tag{9}$$

and

$$i\omega(\mathbf{m} + \alpha \mathbf{m} \times \hat{\mathbf{n}}) = |\gamma|\mu_0 \left(H_{\text{eff}} \mathbf{m} - M_{\text{S}} \mathbf{h}\right) \times \hat{\mathbf{n}}, \tag{10}$$

where $\mathbf{m}(\mathbf{r})$ and $\mathbf{h}(\mathbf{r})$ are the complex amplitudes of dynamic magnetization and dynamic effective field.

2. Magnetic interactions

The magnetic interactions determine both the static magnetic configuration and the coupling between precessing magnetic moments (see Fig. 3). In the magnetic system, we can distinguish two types of interactions: exchange interaction — a short-range of quantum origin and dipolar interaction — a long-range of classical origin. The interplay between the exchange and dipolar interactions is responsible for many unique features of magnonic systems, e.g., complexity and tunability of the magnetic configurations or the lack of the scalability of the spin-wave spectrum with the change of the size of the system. The properties of magnonic systems change significantly with their sizes. The interactions, governing the

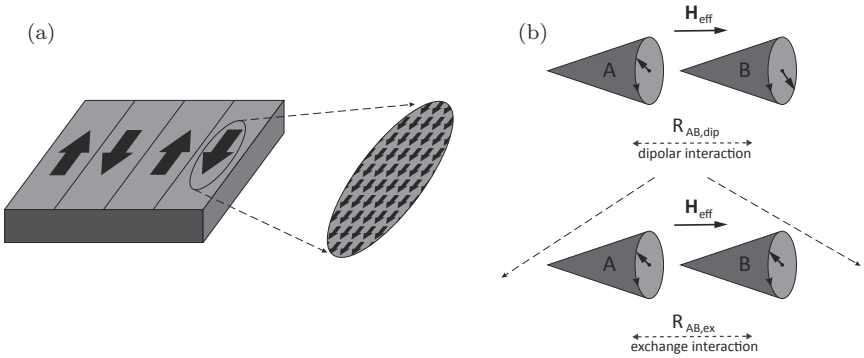

Fig. 3. The interplay between dipolar and exchange interactions. (a) The magnetic domains are oriented anti-parallel which minimize magnetostatic energy. However, at short distances, inside the domains, the exchange interactions prevail, which forces the parallel alignment of the magnetic moment in ferromagnetic material. (b) The in-phase or out-of-phase procession of two magnetic moments A and B is preferred in dependence on the distance R_{AB} between them. The static components of magnetic moments are colinear.

dynamics of magnetization, gradually transit from exchange to a dipolar character when the sizes of the system are expanding from nanometer to micrometer range.

The magnetic interactions are incorporated into the Landau–Lifshitz equation (1) by introducing the spatial- and time-dependent components of the effective magnetic field. The effective field acting on the magnetization at a particular location reflects the impact of all magnetic interactions from the surrounding of selected locations. In this section, we discuss the origin of the terms of effective field describing the exchange and dipolar interaction.

2.1. *Exchange interactions*

The origin of spontaneous magnetization in ferromagnets lies in the parallel alignment of the spin of electrons on lattice sites, and more precisely since electrons are fermions, the Pauli exclusion principle governs the ferromagnetism. This fundamental law says that any two fermions cannot occupy the same quantum state, including degrees of freedom related to the spin. Although the electrons interact electrostatically, the dominant interaction at short

ranges results from the Pauli exclusion principle, which prefers the parallel alignment of electronic spins in ferromagnetic material. Therefore, the exchange interaction between two electrons can be modeled by the Hamitolnian expressed only by electronic spins[29,30]: $\mathcal{H}_{\mathrm{ex},i,j} = -J_{i,j}\mathbf{S}_i \cdot \mathbf{S}_j$. The parameter $J_{i,j}$, called exchange integral, is independent on spin degrees of freedom and expresses the overlap of the electron wave functions located at site i and j. The dimensionless spins: $\mathbf{S}_i$, $\mathbf{S}_j$ are related to the angular momenta: $\hbar\mathbf{S}_i$, $\hbar\mathbf{S}_j$ and the magnetic moments $\gamma\hbar\mathbf{S}_i$, $\gamma\hbar\mathbf{S}_j$. The gyromagnetic ratio $\gamma = g\mu_{\mathrm{B}}/\hbar$ is expressed by the constants: g-factor and Bohr magneton μ_{B}. In a ferromagnet, the exchange interaction is attractive for parallel alignment of spins. Therefore, the exchange integral is positive ($J_{i,j} > 0$). For the atomic lattice of interacting spins we got, so-called, Heisenberg hamiltonian: $\mathcal{H}_{\mathrm{ex}} = -\frac{1}{2}\sum_{ij} J_{i,j}\mathbf{S}_i \cdot \mathbf{S}_j$, where the summation takes place over pairs of nearest neighbors (NN), due to short range of the exchange interaction.

In the classical limit, the exchange energy of selected (macro)spin $\mathbf{S}_i$ is given formally by the same formula as in quantum limit

$$\mathcal{H}_{\mathrm{ex},i} = -\sum_{\substack{j \\ (NN\,\mathrm{of}\,i)}} J_{i,j}\mathbf{S}_i \cdot \mathbf{S}_j. \tag{11}$$

The vectors $\mathbf{S}_i$, $\mathbf{S}_j$ can be oriented arbitrary in space, without the constraints describing the quantization of the angular momentum. Equation (11) is our starting point to formulate the exchange field in the form considered in the classical theory of spin-wave dynamics. To proceed further, we need to put three assumptions:

- the exchange interaction is isotropic ($J_{i,j} = J$ for any pair of NN),
- the angle between $\mathbf{S}_i$ and $\mathbf{S}_j$ is small,
- the spatial distribution of the magnetic moments ($\gamma\hbar\mathbf{S}_i$, $\gamma\hbar\mathbf{S}_j$) can be described by continuous function, namely magnetization vector: $\mathbf{M}(\mathbf{r})$.

The above assumptions allow incorporating the exchange interaction to the classical model of magnetization dynamics in a continuous medium, where the Landau–Lifshitz equation can be used to describe

the precession of magnetization vector. We can then express the exchange energy as a continuous function of the position $\mathbf{r}$ (of the i^{th} magnetic moment) and expand the magnetization into Taylor series to describe the small spatial changes of the orientation of the magnetization vector. Detailed discussion is presented in Ref. [31]. Taking into account all these facts, we can derive the energy density of exchange interaction in the form:

$$\epsilon_{\text{ex}} = \lambda M_{\text{S}}^2 + \frac{A}{M_{\text{S}}^2} \sum_i \left(\partial_{x_i} \boldsymbol{M}\right)^2 . \tag{12}$$

The parameter A is called exchange stiffness constant and can be related to exchange integral: $A = \frac{JS^2 n}{a}$ (for cubic lattices), where $S = |\mathbf{S}_1| = |\mathbf{S}_2|$, a is the lattice constant and $N = n/a^3$ is a number of spins/atoms per unit cell. The saturation magnetization can also be related to microscopic parameters: $M_{\text{S}} = N\mu_{\text{B}} g S$. In the continuous model, the material parameters can be, in general, spatially dependent: $M_{\text{S}}(\mathbf{r})$, $A(\mathbf{r})$. The parameter $\lambda = -\frac{ZJ}{N\mu_{\text{B}}^2 g^2}$ (where Z is the number of NN for the selected spin) describes the static term which can be neglected for the derivation of the exchange field.[31]

In general, the effective field can be calculated by functional differentiation of energy density $\epsilon_{\text{eff}}(\mathbf{M}, \partial_{x_i}\mathbf{M})$ with respect to the magnetization vector[2]

$$\mathbf{H}_{\text{eff}} = -\frac{1}{\mu_0} \frac{\delta \epsilon_{\text{eff}}}{\delta \boldsymbol{M}} = -\frac{1}{\mu_0} \left(\frac{\partial \epsilon_{\text{eff}}}{\partial \mathbf{M}} - \sum_i \partial_{x_i} \frac{\partial \epsilon_{\text{eff}}}{\partial (\partial_{x_i} \mathbf{M})} \right). \tag{13}$$

Here, by calculating the functional derivative of the exchange energy density (12) $\epsilon_{\text{eff}}(\mathbf{M}, \partial_{x_i}\mathbf{M})$ with respect to the magnetization vector, we obtain the following formula for the corresponding contribution to the effective field:

$$\mathbf{H}_{\text{ex}} = \frac{1}{\mu_0} \nabla \left(\frac{2A}{M_{\text{S}}^2} \right) \nabla \mathbf{M}. \tag{14}$$

For uniformly magnetized sample, the static component of exchange field is equal to zero, and the exchange field is expressed only by the

dynamic part, which for the spin-wave of the frequency ω is:

$$\mathbf{H}_{\mathrm{ex}}(\mathbf{r},t) = \mathbf{h}_{\mathrm{ex}}(\mathbf{r})e^{i\omega t} = \frac{1}{\mu_0}\nabla\left(\frac{2A}{M_{\mathrm{S}}^2}\right)\nabla\mathbf{m}(\mathbf{r})\; e^{i\omega t}. \tag{15}$$

It is worth noting that the x, y, z components of the magnetic field in Eqs. (13)–(15) are obtained for the corresponding components of magnetization substituted on the right-hand sides of these equations.

2.2. *Dipolar interactions*

The dipolar interaction can be described using the principles of classical electromagnetism. The energy of dipolar interaction between the pair of spins can be described by the formula derived on the ground of magnetostatics[5]:

$$\mathcal{H}_{\mathrm{ms},i,j} = \mu_0\frac{(g\mu_B)^2}{4\pi}\left(\frac{\mathbf{S}_i\cdot\mathbf{S}_j}{r_{i,j}^3} - 3\frac{(\mathbf{S}_i\cdot\mathbf{r}_{i,j})\,(\mathbf{S}_j\cdot\mathbf{r}_{i,j})}{r_{i,j}^5}\right), \tag{16}$$

where $\mathbf{r}_{i,j}$ is a vector connecting $\mathbf{S}_i$ and $\mathbf{S}_j$. In order to calculate the dipolar energy of ith spin in the magnetic system, we need to sum up the contributions from all remaining spins in the system which means the interaction on the long-range:

$$\mathcal{H}_{\mathrm{ms},i} = \sum_{\substack{j\\(j\neq i)}} \mathcal{H}_{\mathrm{ms},i,j}. \tag{17}$$

It is worth to note that the sum (17) will depend on the shape of the magnetic body (this can be easily checked for uniformly magnetized sample ($\mathbf{S}_j$ = const.). It results from the anisotropy of the dipolar interactions (16) which can be repulsive ($\mathbf{r}_{i,j}\perp\mathbf{S}_i,\mathbf{S}_j$) or attractive ($\mathbf{r}_{i,j}\parallel\mathbf{S}_i,\mathbf{S}_j$), depending on the relative position $\mathbf{r}_{i,j}$ and orientation inside the magnetic body. The formula (16) is also valid for precessing magnetic moments because the retardation effects are weak for the GHz dynamic in micro- and nanoscale. The magnetic dipolar energy and demagnetizing field are practically independent on electric currents and electric fields weakly induced by precessing magnetization. The lack of the feedback from a magnetic field to

an electric field in magnonics means that the electric currents and electric fields can be the sources of the external magnetic field only because they are not involved in the mediation of interactions between magnetic moments.

The derivation of the components of the effective field resulting from the presence of dipolar interaction is quite straightforward in a continuous model, where we consider the spatial distribution of magnetization. In the magnetostatic approximation, the Maxwell equation for the rotation of magnetic field $\mathbf{H}$ reduces to: $\nabla \times \mathbf{H} = 0$. For such field, called magnetostatic field $\mathbf{H}_{\text{ms}}$, we can introduce the scalar potential Φ[1,4]:

$$\mathbf{H}_{\text{ms}} = -\nabla\Phi, \tag{18}$$

called magnetostatic potential. From the other Maxwell equation (Gauss equation for magnetism: $\nabla \cdot \mathbf{B} = 0$) we obtain the Poisson equation or the Laplace equation for magnetostatic potential inside Φ_{in} or outside Φ_{out} the magnetic material, respectively:

$$\begin{aligned} \Delta\Phi_{\text{in}} &= \nabla \cdot \mathbf{M}, \\ \Delta\Phi_{\text{out}} &= 0. \end{aligned} \tag{19}$$

The requirement of the continuity of the normal component of the **B**-field and the tangential component of the **H**-field on the interface leads to the following boundary conditions for magnetostatic potential:

$$\begin{aligned} \Phi_{\text{in}} &= \Phi_{\text{out}}, \\ \frac{\partial\Phi_{\text{in}}}{\partial\hat{\mathbf{n}}_0} - \frac{\partial\Phi_{\text{out}}}{\partial\hat{\mathbf{n}}_0} &= \mathbf{M} \cdot \hat{\mathbf{n}}_0, \end{aligned} \tag{20}$$

where $\hat{\mathbf{n}}_0$ is the unit vector normal to the interface. The magnetostatic potential must be also regular at infinity.[32] It means that both $|r\Phi|$ and $|r^2\Phi|$ must be limited for $r \to \infty$.

The general solution of Eqs. (19) has a form:

$$\Phi(\mathbf{r}) = -\frac{1}{4\pi}\int_V \frac{\nabla' \cdot \mathbf{M}(\mathbf{r}')}{|\mathbf{r}-\mathbf{r}'|}dV' + \frac{1}{4\pi}\oint_S \frac{\hat{\mathbf{n}'}_0 \cdot \mathbf{M}(\mathbf{r}')}{|\mathbf{r}-\mathbf{r}'|}dS'. \qquad (21)$$

The first term in (21) describes the contribution of the volume magnetic charges which appear in non-collinear magnetic configurations where $\nabla \cdot \mathbf{M}(\mathbf{r}) \neq 0$ (it vanishes at strong external field $\mathbf{H}_0$ where the magnetization is saturated). The second term in (21) is related to the presence of surface magnetic charges induced on the interfaces where the normal component of magnetization is discontinuous. It refers also to the surfaces of magnetic body separating magnetic ($\mathbf{M} \neq 0$) and nonmagnetic medium ($\mathbf{M} = 0$).

In the linear approximation, the demagnetizing field $\mathbf{H}_{\mathrm{ms}}(\mathbf{r}, t) = \mathbf{H}_{\mathrm{ms}}(\mathbf{r}) + \mathbf{h}_{\mathrm{ms}}(\mathbf{r})e^{i\omega t}$ can be calculated from the spatial distribution of magnetization considered independently for static $\mathbf{M}(\mathbf{r})$ and dynamic $\mathbf{m}(\mathbf{r}, t)$ components, behind the source of the static and dynamic demagnetizing fields, respectively.

The dipolar interactions are non-local and depend on the geometrical factors: shape and sizes of the magnetic structure. However, the static magnetic configuration is determined not only by the geometry of a magnetic body but also by the external magnetic field. Therefore, the interplay between the geometry and applied field is responsible for forming the static magnetic landscape in which the magnetic interactions couples the precessing magnetic moments. It is worth to note that (dynamic) dipolar interactions between the precessing magnetic moments are also long-range and anisotropic because the dynamic demagnetizing field depends globally on the shape of magnetic sample and the orientation of the external magnetic field.

2.2.1. *Demagnetizing effects in ellipsoidal body*

The static demagnetizing field inside the uniformly magnetized magnetic body of an ellipsoidal shape is uniform.[1,33] Therefore, for magnetic samples in the shape of an ellipsoid (which can be reduced to the sphere, infinitely long cylinder or infinitely extended layer,

for specific values of semi-axes), the relation between demagnetizing field and the magnetization is particularly simple:

$$\mathbf{H}_{\mathrm{ms}} = -\mathcal{N} \cdot \mathbf{M}, \tag{22}$$

where $\mathcal{N}$ is a so-called demagnetizing tensor. The demagnetizing tensor is symmetric and can be reduced to diagonal tensor when defined in the Cartesian coordinate system with the x, y, z-axis being co-linear with the principal axes of the ellipsoid. The relation (22) is also valid for dynamic field and dynamic magnetization for spatially uniform magnetization precession.

For sphere, cylindrical rod (aligned along the x-direction), and layer (perpendicular to the x-direction) the non-zero (i.e., diagonal) coefficients of demagnetizing tensor take values: $N_x = N_y = N_z = \frac{1}{3}$ (sphere), $N_y = N_z = \frac{1}{2}$ (cylindrical rod), $N_x = 1$ (layer). It is worth to note, that the trace of demagnetizing tensor is equal to one[33]: $N_x + N_y + N_z = 1$.

For magnetic bodies of the non-ellipsoidal shape, the demagnetizing tensor can be generalised when we assume its spatial dependence[34] $\mathbf{H}_{\mathrm{ms}}(\mathbf{r}) = -\mathcal{N}(\mathbf{r}) \cdot \mathbf{M}(\mathbf{r})$ which is consistent with the general approach presented in Eqs. (18)–(21).

3. Spin waves in confined geometries

The spin waves were postulated in 1930s by Felix Bloch[35] in order to include the magnetic contribution to the specific heat in macroscopic samples. He showed that the magnetization of a Heisenberg ferromagnet[29] at low temperature should deviate from its zero-temperature value with a $T^{\frac{3}{2}}$ dependence without any external magnetic field applied. This quantum mechanical theory of spin was developed in 1940s using the formalism of the second quantization by Holstein and Primakoff.[36] However, the semiclassical theory of spin waves was initiated even earlier in the mid-1930s, by Heller and Kramers.[37] In this approach, based on classical Landau–Lifshitz equation, the spin wave can be understood as a coherent precession of magnetization in magnetic body, where the differences in phase of precession are acquired gradually with the distance — see Fig. 4.

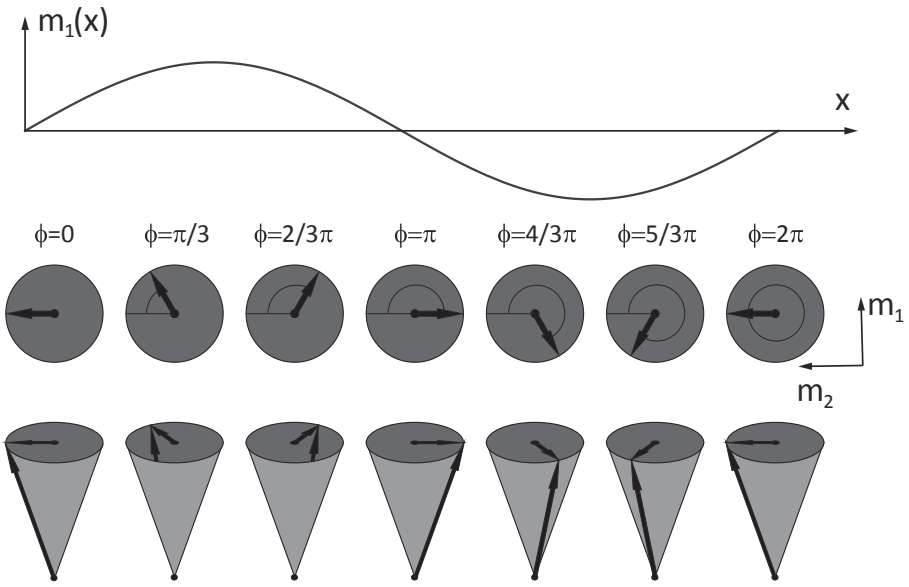

Fig. 4. The harmonic spin-wave visualized as a sequence of precessing magnetic moments. Due to the interactions between the magnetic moments, they can precess coherently, i.e., with the phase difference fixed in time. The phase difference increases with the distance between the magnetic moments. As a result, magnetic moments oscillate in space, forming the spin-wave.

This collective phenomenon is a classical wave, where we observe the oscillation of dynamic components of magnetization both in time (with the precession frequency ω) and space (with wave vector $\mathbf{k}$).

The semiclassical approach appeared to be very effective in the description of spin waves also in confined geometry of nanostructures where the characteristic sizes are in the range of hundreds of nanometres or single micrometers. Due to the long-range and anisotropic character of the dipolar interaction, the properties of spin waves can be shaped by the geometrical factors. The pioneer works concerning the dipolar dominated spin waves in confined geometries of magnetic sphere[38] and layer[39] appeared at the turn of the 1950s and 1960s. The significant increase of the activity on the subject of dipolar-exchange spin waves in confined geometries is observed from the beginning of this century and is related to the development in the fabrication techniques and the progress in numerical simulations. That time,

the term of *magnonics* has been accepted for this new field of research.

3.1. *Uniform oscillations of magnetization*

For the uniform precession of the magnetization in magnetic body of ellipsoidal shape, we can use the demagnetizing tensor to describe both the static and dynamic demagnetizing fields. The corresponding components of the effective field, in the absence of external dynamic field and with exchange interaction neglected, will read

$$\begin{aligned} H_{\text{eff}}\hat{\mathbf{n}} &= \mathbf{H}_0 - M_{\text{S}}\,\mathcal{N}\cdot\hat{\mathbf{n}}, \\ \hat{\mathbf{h}} &= -\mathcal{N}\cdot\mathbf{m}. \end{aligned} \tag{23}$$

The static external field $\mathbf{H}_0$ is not co-linear with the static magnetization $M_{\text{S}}\hat{\mathbf{n}}$ due to the presence of static demagnetizing field $-M_{\text{S}}\mathcal{N}\cdot\hat{\mathbf{n}}$. The static magnetization $M_{\text{S}}\hat{\mathbf{n}}$ is aligned along the direction of static component of effective field $H_{\text{eff}}\hat{\mathbf{n}}$ which is ensured by canceling the torque $\mathbf{T} = \hat{\mathbf{n}}M_{\text{S}} \times (\mathbf{H}_0 - M_{\text{S}}\,\mathcal{N}\cdot\hat{\mathbf{n}}) = 0$. It means, that all the components of the external field perpendicular to the direction of effective field $\hat{\mathbf{n}}$ are canceled by demagnetizing field.

The linearized Landau–Lifshitz equation can be then written in the following form:

$$i\omega\mathbf{m} = |\gamma|\mu_0\Big[\Big(\big(\mathbf{H}_0\cdot\hat{\mathbf{n}} - M_{\text{S}}(\mathcal{N}\cdot\hat{\mathbf{n}})\cdot\hat{\mathbf{n}}\big)\mathbf{m} + M_{\text{S}}(\mathcal{N}\cdot\mathbf{m})\Big] \times \hat{\mathbf{n}}, \tag{24}$$

which can be expanded into set of the equations for the components m_1 and m_2 of the dynamic magnetization $\mathbf{m} = [m_1, m_2, 0]$:

$$\begin{aligned} -\left(\omega_H + \omega_{\text{M}}\mathcal{N}_{11}\right)m_1 + \left(i\omega + \omega_{\text{M}}\mathcal{N}_{12}\right)m_2 = 0, \\ \left(i\omega + \omega_{\text{M}}\mathcal{N}_{21}\right)m_1 + \left(\omega_H + \omega_{\text{M}}\mathcal{N}_{22}\right)m_2 = 0. \end{aligned} \tag{25}$$

The symbols: $\omega_{\text{M}} = |\gamma|\mu_0 M_{\text{S}}$ and $\omega_{\text{H}} = |\gamma|\mu_0(\mathbf{H}_0\cdot\hat{\mathbf{n}} - M_{\text{S}}\mathcal{N}_{nn})$ denotes the values of the magnetization saturation M_{S} and the static component of effective field expressed in the unit of magnetic field (the index n denotes the direction of static magnetization). Equations (25) form the homogeneous set for m_1 and m_2, for which

the determinant should be equal to zero to get nontrivial solutions. This condition gives the equation for the eigenfrequencies of spin-wave processions

$$\omega = \sqrt{(\omega_{\mathrm{H}} + \omega_{\mathrm{M}}\mathcal{N}_{11})(\omega_{\mathrm{H}} + \omega_{\mathrm{M}}\mathcal{N}_{22}) - \omega_{\mathrm{M}}^2\mathcal{N}_{12}}, \tag{26}$$

where we use the symmetry of demagnetizing tensor: $\mathcal{N}_{12} = \mathcal{N}_{21}$. If the external field is applied along one of the principal axes of the ellipsoid, then in the Cartesian coordinate system with the z-axis oriented in $\hat{\mathbf{n}}$ direction, Eq. (25) reduces to formula derived by Kittel[40]

$$\omega = |\gamma|\mu_0\sqrt{\big(H_0 + (\mathcal{N}_x - \mathcal{N}_z)M_{\mathrm{S}})(H_0 + (\mathcal{N}_y - \mathcal{N}_z)M_{\mathrm{S}})\big)}. \tag{27}$$

The Kittel equation can take the following form for selected cases:

$$\begin{aligned}
&\omega = |\gamma|\mu_0 H_0 && \text{for sphere,}\\
&\omega = |\gamma|\mu_0\left(H_0 + \frac{1}{2}M_{\mathrm{S}}\right) && \text{for cylindrical rod: } \mathbf{H}_0 \text{ along the rod,}\\
&\omega = |\gamma|\mu_0\sqrt{H_0(H_0 + M_{\mathrm{S}})} && \text{for layer: } \mathbf{H}_0 \text{ in the plane.}
\end{aligned} \tag{28}$$

Due to large wavelength of electromagnetic waves (compared to the wavelength of spin waves of the same frequency), the absorption of the radiofrequency field by spin waves is the largest for uniform precession (for Kittel modes (2)), where the wavelength is infinite. It results from the fact that the coupling between spin-wave and electromagnetic wave depends on the spatial overlap of dynamic magnetization and the dynamic applied field $\mathbf{h}_0$: $\int_{\mathrm{volume}} \mathbf{m}(\mathbf{r}, t) \cdot \mathbf{h}_0(\mathbf{r}, t)d\mathbf{r}$.

3.2. *Spin waves*

The spin-wave modes are quantized in the dimensions which are constrained — their wave vectors (wavelength) take the discrete values along these dimensions, and the frequencies are numbered by integer indexes. The spin-wave modes in ferromagnetic spheres were analyzed in details by Walker in late 1950s[38] in dipole dominated

regime. The frequencies ω of the spin-wave eigenmodes in the sphere are the solution of the equation:

$$(n+1) + \xi_0 \frac{\frac{d}{d\xi_0} P_n^m(\xi_0)}{P_n^m(\xi_0)} + m\,\nu = 0, \tag{29}$$

where $\xi_0 = 1/\delta + 1$ and $\delta = \omega_{\mathrm{H}}\omega_{\mathrm{M}}/(\omega_{\mathrm{H}}^2 - \omega^2)$, $\nu = \omega\omega_{\mathrm{M}}/(\omega_{\mathrm{H}}^2 - \omega^2)$. The functions $P_n^m(\xi_0)$ are the associated Legendre polynomials indexed by positive integer n and the integer $\pm m = 0, \ldots, n$. Due to 3D confinement the spin-wave modes will be indexed by three integers (n, m, r),[41,42] where $r - 1$ is the number of solutions of Eq. (29). The index r denotes the number of nodes of spin-wave mode in radial direction (perpendicular to the direction of static effective field $\hat{\mathbf{n}}$), whereas the value $n - m - 2r$ is the number of zeros of the modes in vertical direction (along the direction of static effective field). The quantization of the modes in azimuthal direction (number of phase rotation around the $\hat{\mathbf{n}}$) is given by the index m. The stronger interaction of these modes (called Walker modes) with electromagnetic waves is observed for the following sets of indexes $(n, n, 0)$ and $(n, n-1, 0)$, for which the eigenfrequencies have a simple linear dependence on the applied field:

$$\begin{aligned} \omega &= \omega_{\mathrm{H}} + \omega_{\mathrm{M}} \frac{n-1}{2n+1} \quad \text{for } (n, n, 0), \\ \omega &= \omega_{\mathrm{H}} + \omega_{\mathrm{M}} \frac{n}{2n+1} \quad \text{for } (n, n-1, 0). \end{aligned} \tag{30}$$

Let us consider the geometry of a ferromagnetic film — a basic structure which can be used to build the magnonic (or photonic-magnonic) crystals by periodic repetition. In this geometry, the spin waves are confined in one dimension only. Therefore, their eigenfrequencies and the profiles of eigenmodes will be indexed by one integer n (describing the quantization in out-of-plane direction — counting the number of nods) and continuous parameter — 2D wave vector $\mathbf{k}$ (describing the propagation in in-plane directions). The strongest coupling with uniform external microwave film is observed for the spatially uniform modes of the eigenfrequencies given by the Kittel equation (27): $\omega = \sqrt{\omega_{\mathrm{H}}(\omega_{\mathrm{H}} + \omega_{\mathrm{M}} \sin^2\theta)}$, where θ is the angle

between the normal to the layer $\hat{n}_0$ and the direction of static effective field $\hat{n}$.

For non-zero wave vector $\mathbf{k} > 0$, the general formula for eigenfrequency of spin wave modes propagating in the thin layer was derived by Kalinikos and Slavin[3,43,44]:

$$\omega = \sqrt{\omega_{\mathrm{H},n}\left(\omega_{\mathrm{H},n} + \omega_{\mathrm{M}} F_n(\theta, \varphi, kd)\right)}, \tag{31}$$

where

$$F_n(\theta, \varphi, \kappa) = P_n(\kappa) + \sin^2\theta \times \left[1 - P_n(\kappa)\left(1 + \cos^2\varphi\right) + \frac{\omega_{\mathrm{M}}}{\omega_{\mathrm{H},n}} P_n(\kappa)\big(1 - P_n(\kappa)\big)\sin^2\varphi\right]. \tag{32}$$

The symbol φ denotes the angle between the direction of the wave vector $\mathbf{k}$ in the plane of the film and the projection of the external magnetic field on these plane. The parameter $\kappa = kd$ is the dimensionless length of the vector $\mathbf{k}$ multiplied by the thickness of the film d.

In the absence of surface anisotropy, there is no additional torque acting on precessing magnetization vector on both surfaces of the film, and their dynamic components are completely unpinned there: $\nabla\mathbf{m}(\mathbf{r}) \cdot \hat{\mathbf{n}}_0 = 0$. For such boundary condition, the spin-wave is quantized inside the film with the wavelength $\lambda_n = \frac{2\pi}{n}d$. Therefore, we introduce the dimensionless parameters $\kappa_n = n\pi$, being of a quantized, out-of-plane component of the wave vector $n\pi/d$, multiplied by the thickness of the layer d.

The dispersion relation (31) and (32) includes the exchange interaction incorporated as an additional term to ω_{H}: $\omega_{\mathrm{H},n} = \omega_{\mathrm{H}} + |\gamma|\frac{2A}{M_{\mathrm{S}}d^2}(\kappa^2 + \kappa_n^2)$, which can be recognized as the exchange dynamic field $|\gamma|\mu_0 h_{\mathrm{ex}}(\mathbf{r})$ expressed in the units of frequency ω. It can be derived from the definition of dynamic exchange field (13) for the spin-wave in the form of plane wave (in the in-plane direction) and unpinned standing waves (in the out-of-plane direction): $\mathbf{m}(\mathbf{r}) = \mathbf{m}\, e^{i(\mathbf{k}\cdot\mathbf{r}_\parallel + \frac{n\pi}{d}x_\perp)}$, where $\mathbf{r}_\parallel$ and $x_\perp$ are the in-plane and out-of-plane components of position vector: $\mathbf{r} = \mathbf{r}_\parallel + x_\perp\hat{\mathbf{n}}_0$.

The function $P_n(\kappa)$ includes the impact of the dipolar interactions resulting from the finite wavelength. It ranges from 0 to 1, depending on the values of both components of the wave vector. For the modes which are uniform across the film ($n = 0$), this function takes the particularly simple form:

$$P_0(\kappa) = 1 - \frac{1 - e^{-\kappa}}{\kappa}, \tag{33}$$

which is equal to zero for $\kappa \to 0$ and reduces Eq. (31) to the formula for ferromagnetic resonance frequency (FMR) frequency. The formulas describing $P_n(\kappa)$ for higher modes ($n > 0$), and taking into account the arbitrary spin-wave pinning on the surfaces of the film, can be found in Ref. [44].

Equation (31) has a form of wave dispersion relation $\omega(\mathbf{k})$ which is a fundamental characteristic describing the propagation of waves. The spin-wave group velocity $\mathbf{v}_{\mathrm{gr}} = \nabla_{\mathbf{k}}\omega$ is the measure of the strength of the dynamic interactions between the precessing magnetic moments. The large values of v_{gr} means that even small phase difference between precessing magnetic moments (or the small change of wave vector) is not indifferent to the system, and is reflected in the significant change of the eigenfrequency of the mode.

The dipolar interactions are anisotropic which is manifested in Eq. (31) by the dependence of the frequency of the spin waves on the orientation of the wave vector, described by the angle φ. For in-plane oriented static magnetization ($\theta = \pi/2$), we observe the distinctive difference between two configurations: $\varphi = 0$ (when $\mathbf{k}$ is parallel to the static magnetization) and $\varphi = \pi/2$ (when $\mathbf{k}$ is perpendicular to the static magnetization). For $\varphi = 0$ the slope of the dispersion relation is negative, and the sign of the phase velocity $\mathbf{v}_{\mathrm{ph}} = \mathbf{k}\,\omega/k^2$ is opposite to the sign of the group velocity v_{ph}, so in this direction the carrier wave of the spin-wave package travels in the opposite direction to the movement of its envelope. For $\varphi = \pi/2$ the signs of v_{ph} and v_{gr} are the same. The dipolarly dominated spin waves in the first configuration ($\varphi = 0$) are called backward waves, whereas the spin waves observed in the following configuration ($\varphi = \pi/2$) are named Damon–Eshbach waves after their discoverers.[39]

In the homogeneously magnetized sample, the presence of the surfaces (or interfaces) which delimits regions of the spin-wave confinement is crucial for the induction of dynamic dipolar field. There is no dynamic dipolar coupling in unconstrained and homogeneously magnetized magnetic material, and therefore the spin wave dispersion relation is flat in dipolar dominated regime $v_{\mathrm{gr}} = 0$. In infinitely extended and uniform magnetic system the spin-wave cannot carry the information and energy unless the exchange interactions start to play a notable role.

4. Magnonic crystals

A popular method of tailoring the flow of waves, beyond the capabilities of uniform media, is a periodic patterning of a system. The periodical modulation of the material properties is a well-known concept in photonics, proposed separately by Yablonovich and John in 1987[45,46] who considered the periodical variation of the dielectric constant.

The same idea can be utilized in the case of spin waves by a periodic modulation of the magnetic properties (i.e., the parameters influencing spin-wave spectra). The first theoretical utilization of a periodical arrangements of ferromagnetic materials in order to control spin-waves dynamics has been demonstrated already 40 years ago for the long-wavelength magnetostatic spin-waves.[47,48] However, artificial, periodic ferromagnetic structures, a magnonic counterpart of photonic crystals, have been started to be named as magnonic crystals only in the 90s[49–51] when the interest in the study of periodic structures for different types of excitations was regrown after the discovery of photonic crystals[45,46] combined with the development of both technologies of nanopatterned structures fabrication suitable for spin-wave propagation and the development of measurement techniques allowing spin-wave detection.

Compared to uniform magnetic systems, one of the main advantages of magnonic crystals is the easiness of obtaining a complex spin-wave spectra with forbidden frequency gaps that can be tailored

by the structural and material parameters. Until now, various types of magnonic crystals have been studied,[13] for instance: periodic arrangements of magnetic stripes or dots coupled via dipolar[52,53] or exchange interactions,[54–57] periodic arrays of holes,[58,59] bicomponent magnonic crystals,[60] or periodic magnetic domain arrangements.[61] In the following subsections, the fundamental theory of wave propagation in periodic media will be introduced. Then, an exemplary magnonic crystal constituting of dipolarly coupled magnetic wires will be analyzed.

4.1. *Bloch theorem*

Historically, the study of ordinary differential equations in the periodic potential was initiated by Gaston Floquet in 1883.[62] The field of mathematics related to that is called after his name Floquet theory with the main theorem known as the Floquet theorem. The solid-state counterpart of that theorem introduced in 1929 by Felix Bloch,[63] is nowadays referred to as the Bloch's theorem. Historically, it was first established for electronic wavefunction in a perfect crystal (with a perfectly periodic potential). However, this theorem is valid for all excitations being solutions of the wave equation in a periodic potential, with magnons among them, as well.

The Bloch's theorem[30] states that the wavefunction ψ (called Bloch wave) of an excitation (e.g., electron, phonon, or magnon) within a perfectly periodic potential (medium) can be written in the following form:

$$\psi(\mathbf{r}) = e^{i\mathbf{k}\cdot\mathbf{r}}u(\mathbf{r}),$$

where the function $u(\mathbf{r})$ is periodic with the same periodicity as the crystal lattice, i.e., $u(\mathbf{r}) = u(\mathbf{r} + \mathbf{a})$, $\mathbf{a}$ is the lattice vector. According to the Bloch's theorem, the Bloch wave is periodic in the reciprocal space:

$$\psi(\mathbf{k}) = \psi(\mathbf{k} + \mathbf{G}),$$

where $\mathbf{G}$ is the reciprocal lattice vector, and $\mathbf{k}$ is the wave vector. The same periodicity show the eigenvalues (energies or frequencies) corresponding to the Bloch functions. For eigenfrequencies we can write:

$$\omega(\mathbf{k}) = \omega(\mathbf{k} + \mathbf{G}), \tag{34}$$

which means that the dispersion relation $\omega(\mathbf{k})$ is periodic in reciprocal space.

4.2. *One-dimensional magnonic crystals*

In order to illustrate how the periodicity of the structure affects the dispersion $\omega(\mathbf{k})$ of spin waves, let us first discuss the consequences of Bloch's theorem on the example of the dispersion relation of the uniform magnetic media after assumption of an artificial periodicity. Then, the one-dimensional magnonic crystal in the form of a periodic in-plane arranged sequence of magnetic stripes will be studied. The latter structure can be considered to be derived from the homogeneous magnetic layer discussed in the earlier section.

4.2.1. *Empty lattice model*

An intriguing example demonstrating the Bloch's theorem is the *empty lattice model* assuming an artificial periodicity in a homogeneous medium.

Let us here consider the dispersion relation of spin waves in the infinite 50-nm thick film made of Py magnetized to the saturation by the external magnetic field of value $\mu_0 H = 0.05$ T directed along the y-axis and spin-wave propagation along the x-axis ($\mathbf{k} = \hat{\mathbf{x}}k$). This dispersion is presented in Fig. 5 by the solid thick black line. The application of the Bloch's theorem duplicates and shifts the primary dispersion (of the thin film) by the multiple of the reciprocal vector, i.e., nG, where $G = \pm 2\pi/a$ and n is an integer (see the solid thin gray lines). The highlighted region of the dispersion of width equal to G and located around $k = 0$ is known as the first Brillouin zone

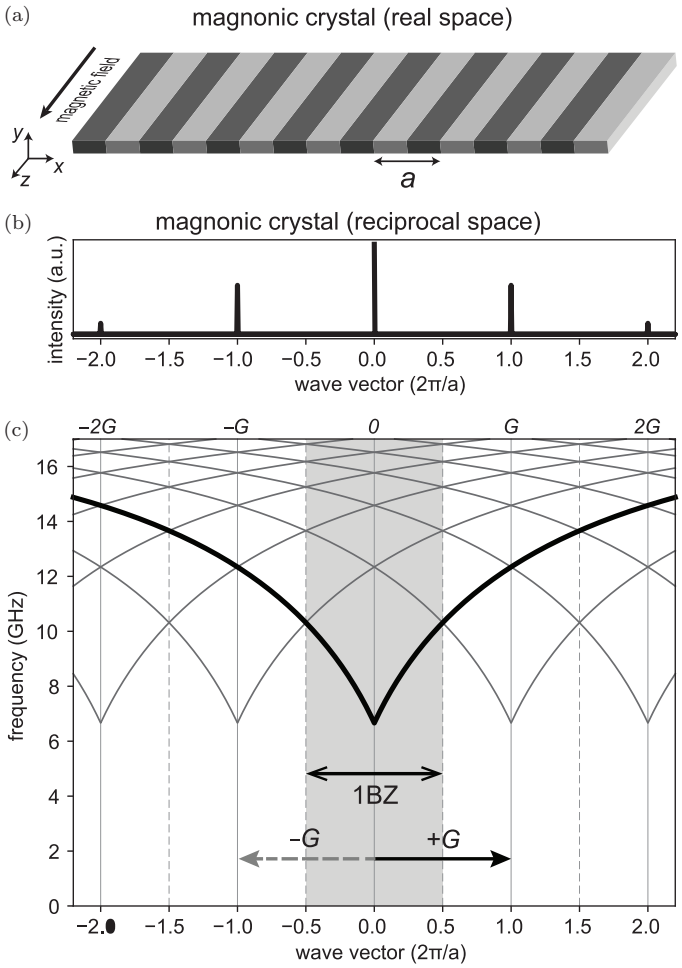

Fig. 5. (a) Exemplary magnonic crystal where darker and lighter regions represent two materials constituting it. (b) Magnonic crystal from (a) plotted in the reciprocal space (after performing *Fast Fourier Transform*), the apparent peaks mark the periodicity of the structure in the reciprocal space — the distance between them is equal to $G = 2\pi/a$ and the most prominent peak is located in the center of the first BZ. (c) Magnonic band structure in 50-nm thick Py film magnetized along the y axis by the external magnetic field of value $\mu_0 H_0 = 0.05$ T in the empty-lattice model fulfilling the Bloch's theorem for the artificial periodicity of $a = 500$ nm. The thick solid black line corresponds to the dispersion of Damon–Eshbach configuration, whereas the black thin solid gray lines are accordingly shifted of that dependence in order to fulfill the Bloch's theorem.

(1BZ). Note that in the empty-lattice model an artificial periodicity is assumed and, therefore, the bands are degenerated at the Brillouin zone boundary ($k = \pi/a$) and at the center of Brillouin zone ($k = 0$). These degeneracies can be removed when real periodicity (periodic modulation of any magnetic properties of media) is assumed. For instance, a consideration of a magnonic crystal consisting of two (or more) materials with different magnetic properties (e.g., Co and Py) or periodic pattern of grooves (film's thickness modulation) can lead to the formation of band gaps in the regions of degeneracy in the empty-lattice model. However, in the subsequent part of the chapter, a different example as a demonstration of a 1D magnonic crystal will be presented.

4.2.2. *Example of 1D magnonic crystal — periodic array of Py stripes separated by air gaps*

Let us consider here, as an example, the magnonic crystals composed of Py wires separated by air gaps in such a manner that the lattice constant is kept the same ($a = 500$ nm) and the widths of wires and air gaps between them are changed. The spin-wave dispersion relations for three ratios between the width of wire and the width of the gap (equal to 490 nm:10 nm; 450 nm:50 nm; 400 nm:100 nm) are presented in Figs. 6(b)–(d) and compared to the dispersion for homogeneous layer of Py with artificially introduced unit cell of 500 nm (lattice constant), see Fig. 6(a). The presented results are obtained for material parameters of Py: saturation magnetization $M_{\mathrm{S}} = 860$ kA/m and exchange constant $A = 13$ pJ/m. In Fig. 6, the homogeneous layer of Py is changed into a magnonic crystal by the introduction of very narrow air gaps into the unit cell. It is easy to see how the spin-wave dispersion relation transforms with increasing the width of the air gaps separating Py wires. A couple of effects typical for magnonic crystals can be seen with the air gap widening: (i) the widths of band gaps increase; (ii) the bands are getting narrower and are characterized by smaller group velocity; (iii) the FMR frequency increases and bottom of the bands shifts to the higher frequencies (which is exceptionally well visible at $k = 0$).

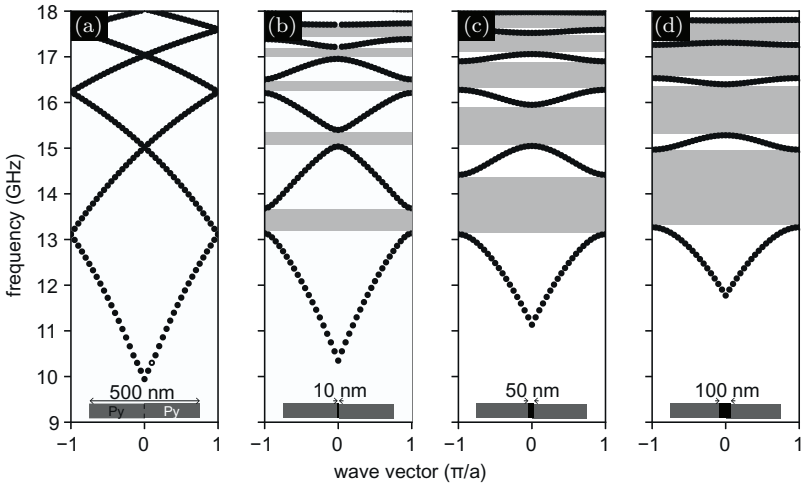

Fig. 6. Dispersion relations calculated for a 30-nm thick Py-based magnonic crystals with the lattice constant of 500 nm and following material parameters: saturation magnetization $M_S = 860\,\mathrm{kA/m}$ and exchange constant $A = 13\,\mathrm{pJ/m}$. On this figure are presented the dispersion relations of (a) uniform Py film (obtained by empty-lattice model), followed by magnonic crystals composed of Py stripes of the same dimensions, separated by (b) 10 nm, (c) 50 nm, and (d) 100 nm air gaps. Light grey regions indicate frequency bandgaps. In the insets are presented unit cells of the calculated structures with the air gaps marked by black color. The presented results are obtained numerically with the help of Finite Element Method in the frequency domain and real space. For this purpose, we have implemented Landau–Lifshitz equation coupled with the Gauss equation for magnetism in the mathematical module of COMSOL Multiphysics. For more details regarding used method please check for example Refs. [57, 64–66].

5. Photonic–magnonic crystals

The exemplary structure of a photonic–magnonic crystal, is presented in Fig. 7. The considered structure is composed of thick (d_m =7 μm) magnetic layers periodically interleaved by relatively thin (d_d = 1.9 μm) non-magnetic spacers which can ensure the dipolar coupling for spin waves confined in the magnetic layers. The magnetic layer is made of dielectric ferrimagnet: yttrium-iron garnet (YIG) $Y_3Fe_5O_{12}$ whereas the non-magnetic spacers are the photonic crystals of finite number of subperiods N composed of TiO_2 and SiO_2 thin layers. YIG is transparent for electromagnetic waves and is characterized by minor spin-wave damping. Therefore, the

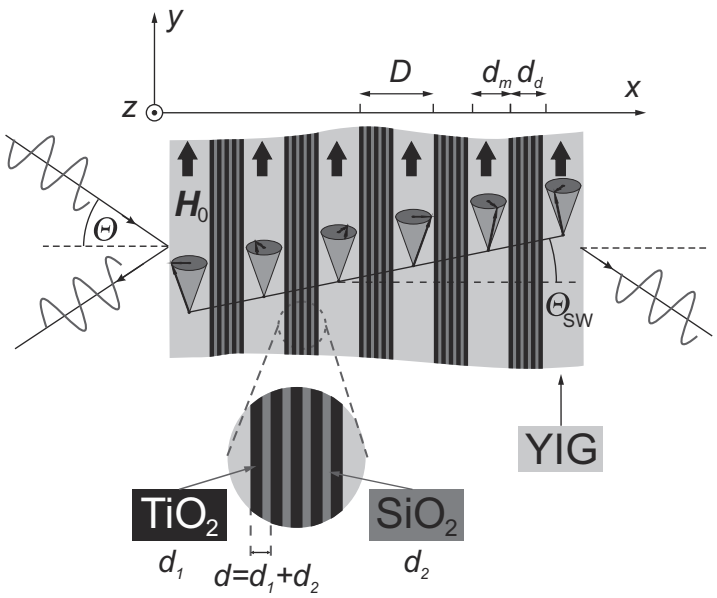

Fig. 7. The considered 1D photonic–magnonic crystal is acting as a magnonic and photonic crystal. The parameters d_{m}, d_{d} and $D = d_{\mathrm{m}} + d_{\mathrm{d}}$ denote the thicknesses of magnetic layers, the thickness of complex non-magnetic layers and the period of the whole structure, respectively. We assume that the external magnetic field H_0 is applied along the y-direction and is sufficiently strong to saturate magnetization in the YIG layers. The non-magnetic layer has an internal structure, as shown in the inset. It has a form of the stack of TiO_2 and SiO_2, d_1 and d_2 stand for their thicknesses, respectively.

electromagnetic waves can be localized inside the magnetic layers where the spin-waves oscillate for long time. It takes place for the frequencies from band gaps of $TiO_2|SiO_2$ photonic crystal, where its finite sections act as Bragg mirrors.

5.1. *Spin-wave dispersion relation*

The spin waves perceive the complex structure presented in Fig. 7 as simple magnonic crystal where the infinitely extended magnetic layers are arranged periodically in the stack, separated by the dielectric spacer. The spacers (i.e., the section of $TiO_2|SiO_2$ photonic crystal) break the exchange interactions between magnetic layer but sustain the dipolar coupling, provided by the dynamic demagnetizing field

penetrating the non-magnetic medium. The exchange interactions are limited only to the interior of each magnetic layer. Therefore, the propagation of spin waves between subsequent magnetic layers is possible, thanks to the long-range dipolar interactions.

In order to analyze the spin-wave dynamics in considered photonic–magnonic crystal let us calculate the spin-wave dispersion relation.

5.1.1. *Model*

The spin-wave dynamics is investigated in the frame of a continuous model based on the Landau–Lifshitz equation. The linearized Landau–Lifshitz equation for the stack of dipolarly coupled, in-plane magnetized infinite layers reads:

$$\begin{aligned} i\frac{\omega}{|\gamma|\mu_0 H_0} m_z(\mathbf{r}) &= m_x(\mathbf{r}) - \frac{M_{\mathrm{S}}(x)}{H_0} \\ &\quad \times \left(\frac{\partial}{\partial x} \lambda_{\mathrm{ex}}^2(x) \frac{\partial}{\partial x} m_x(\mathbf{r}) - \lambda_{\mathrm{ex}}^2(x)(k_y^2 + k_z^2) m_x(\mathbf{r}) \right) \\ &\quad - \frac{M_{\mathrm{S}}(x)}{H_0} h_{\mathrm{ms}_x}, \\ i\frac{\omega}{|\gamma|\mu_0 H_0} m_x(\mathbf{r}) &= -m_z(\mathbf{r}) + \frac{M_{\mathrm{S}}(x)}{H_0} \\ &\quad \times \left(\frac{\partial}{\partial x} \lambda_{\mathrm{ex}}^2(x) \frac{\partial}{\partial x} m_z(\mathbf{r}) - \lambda_{\mathrm{ex}}^2(x)(k_y^2 + k_z^2) m_z(\mathbf{r}) \right) \\ &\quad + \frac{M_{\mathrm{S}}(x)}{H_0} h_{\mathrm{ms}_x}, \end{aligned} \tag{35}$$

where the parameter $\lambda_{\mathrm{ex}} = \sqrt{2A/(\mu_0 M_{\mathrm{S}})}$ is so-called exchange length. Equation (35) must be completed by the formula for the x- and z-components of the dynamic demagnetizing field, $\mathbf{h}_{\mathrm{dm}}$:

$$\begin{aligned} h_{\mathrm{dm},z} &= -\sum_G \frac{k_z^2 m_z(G) + k_z(k_x + G) m_x(G)}{\kappa^2} e^{-i\boldsymbol{\kappa}\cdot\mathbf{r}}, \\ h_{\mathrm{dm},x} &= -\sum_G \frac{(k_x + G)^2 m_x(G) + k_z(k_x + G) m_z(G)}{\kappa^2} e^{-i\boldsymbol{\kappa}\cdot\mathbf{r}}. \end{aligned} \tag{36}$$

The formulas (36) are found form Maxwell equations in magnetostatic approximation by the expansion of the dynamic component of magnetization (being a Bloch function) in the Fourier series:

$$m_{x,z}(\mathbf{r}) = \sum_G m_{x,z}(G) e^{i\kappa\cdot\mathbf{r}}, \tag{37}$$

where $\kappa = [k_x + G, k_y, k_z]$ and $G = n\pi/D$ is the reciprocal lattice vector for the one-dimensional lattice of the periods $D = d_\mathrm{m} + d_\mathrm{d}$, $(n = 0, \pm 1, \pm 2, \ldots)$.

The material parameters $M_\mathrm{S}(\mathbf{r})$ and $\lambda_\mathrm{ex}(\mathbf{r})$ are periodic and can be expanded in the Fourier series as well

$$M_\mathrm{S}(x) = \sum_G M_\mathrm{S}(G) e^{iGx}, \;\; \lambda_\mathrm{ex}(x) = \sum_G \lambda_\mathrm{ex}(G) e^{iGx}. \tag{38}$$

Such an expansion allows to transform two differential equations (35) into the set of algebraic equations for Fourier components $m_x(G)$ and $m_z(G)$. This set of equations has a form of the algebraic eigenvalue problem (with the eigenvalues being the eigenfrequencies ω of spin-wave modes) and can be solved numerically for a fixed value of the wave vector $\mathbf{k}$. By solving the eigenvalue problem for the successive values of $\mathbf{k}$, we can plot the branches dispersion relation: $\omega(\mathbf{k})$ and discuss the spin-wave dynamics in the considered photonic–magnonic crystal.

The presented computational method, based on the Fourier expansion of the Bloch waves (solutions) and the material parameters (coefficients of linear differential equations), is called plane wave method and is widely used to calculate the dispersion relation for the Bloch waves in periodic media.

5.1.2. *Results*

Spin waves can propagate between magnetic layers separated by nonmagnetic spacers due to the dynamic demagnetizing field, which couples the precessing magnetic moments at a distance. The magnetic film can be magnetized in the out-of-plane direction in the presence of strong out-of-plane anisotropy, or strong external field applied perpendicularly to the plane of the film. However, for such

configuration, the dynamic components of magnetization are oriented in-plane and do not produce any surface charges. Therefore, the dynamic demagnetizing field can be produced only by the volume charges which emerge for non-uniform precession of magnetization in the film. This non-uniform precession can be achieved by the spin waves propagation in the plane of a film with the non-zero wave vector components k_y or k_z. We considered here the case where the static magnetization is oriented in-plane due to the shape anisotropy of the magnetic layers. For such a geometry, the out-of-plane magnetization produces the dynamic demagnetizing field $h_{\mathrm{dm},x} = -m_x$, but it can not couple the magnetization between the films. The efficiency of the dynamical coupling between the magnetic layers can be observed in the situation when some components of the spin waves are propagating in the in-plane direction. So, in the considered system, spin waves can propagate through the layers (with non-zero group velocity) only in the case of an oblique propagation to the normal of the layers.

For the considered configuration, the impacts of the (plane wave) components of spin waves, parallel or perpendicular to the direction of the in-plane applied external field H_0 (described by k_y or k_z), on the propagation of (Bloch) spin waves in the x-direction are distinguishable. Both y-and z-components of the spin-wave contribute differently to the dynamic demagnetising field (36). This field is, in turn, responsible for the propagation of the spin-wave (in the form of Bloch wave) between periodically placed magnetic layers. In Fig. 8(a), we presented the spin-wave dispersion relation showing the propagation in the direction of periodicity (i.e., in the x-direction). The two lowest dispersion branches are strongly dispersive (have a significant slope, indicating noticeable group velocity) due to the dynamic dipolar interactions induced by the presence of the non-zero y-component of the spin-wave. The direction of the wave vector is here oblique, deflected by the angle $\theta_{\mathrm{SW}} = \mathrm{atan}(k_y/k_x)$ from the normal direction. For the higher branches, the exchange interaction starts to dominate, but this type of interaction is limited to the interior of the magnetic layers. Due to the lack of the exchange coupling between the magnetic layers, the higher

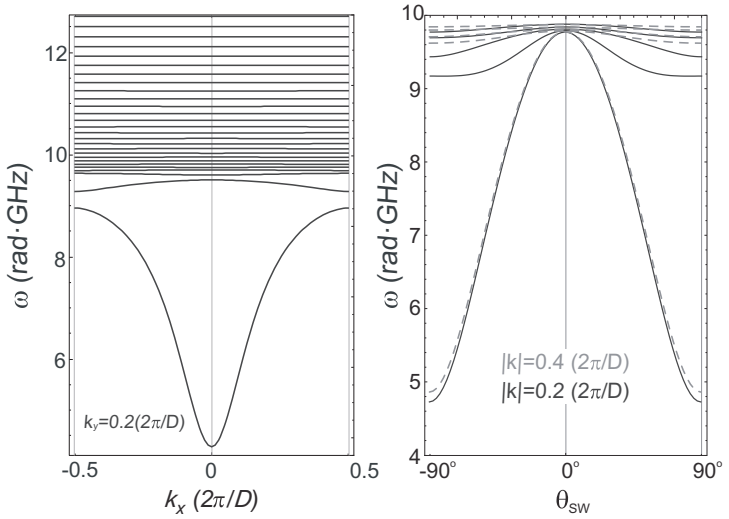

(a) (b)

Fig. 8. (a) Spin waves spectrum for the photonic–magnonic crystal ($d_{\mathrm{m}} = 7\ \mu$m, $d_{\mathrm{d}} = 1.9\ \mu$m) with the external magnetic field of value $\mu_0 H_0 = 10$ mT applied in the plane of layers (along the y-axis). The non-zero in-plane wave vector ($k_y = 0.2\frac{2\pi}{D}$, k_z=0) component induces the non-vanishing dynamical demagnetizing field along with the periodicity of the system which couples the spin waves across the non-magnetic dielectrics and allows the formation of the propagating modes in the first and second band. (b) The dependence of the lowest eigenfrequencies on the direction of the spin-wave propagation (θ_{SW} means the angle between the direction of propagation of spin waves and normal to the interfaces).[19]

exchange dominated branches are flat. In order to investigate how the contribution of the in-plane y-component of the spin-wave affects the propagation in the x-direction, we fixed the length of the wave vector $|k| = \sqrt{k_x^2 + k_y^2}$ and changed the angle θ_{SW}. In Fig. 8(b), we can see that for $\theta_{\mathrm{SW}} \to 0$ the lowest (dispersive) modes are shifted up towards the frequencies of (dispersionless) exchange dominated modes. It shows that for the propagation in the normal direction, the dispersion branches become flat because the coupling between the magnetic layer is reduced.

Regardless of the coupling between the magnetic layers, the magnetization dynamics take place only there. So, in order to enhance the interaction between spin waves and electromagnetic

waves, the electromagnetic waves in the magnetic layers should be confined, as well. In order to achieve this goal, the spectral properties of electromagnetic waves in photonic-magnonic crystal should also be investigated.

5.2. *Electromagnetic wave transmission*

Now let us consider transmission of electromagnetic waves through the photonic–magnonic crystal presented in Fig. 7(b). For electromagnetic waves this structure can be treated as a magneto-photonic crystal with double periodicity: with the subperiod $d = d_1 + d_2$ inside the dielectric photonic crystal layer composed of N layers of TiO_2 and SiO_2 and the period D of the alternating YIG and dielectric photonic crystal layers. We assume that each dielectric composite layer of thickness d_d consists of N subperiods of thickness $d = d_1 + d_2$ and additional sublayer of TiO_2, so the thickness of the dielectric composite layer is $d_\mathrm{d} = Nd + d_1$, as shown in Fig. 7(a). Further we will change the number of the unit cells N, assuming that the thickness of the composite dielectric layer d_d is fixed and does not change with the increasing number N. We choose the dielectric sublayer thicknesses to be in proportion $d_1/d_2 = 2/3$, so the dielectric sublayer thicknesses are $d_1 = 2d_\mathrm{d}/(5N + 2)$ and $d_2 = 3d_\mathrm{d}/(5N + 2)$. The photonic–magnonic crystal structure consists of M periods of thickness $D = d_\mathrm{m} + d_\mathrm{d} = d_\mathrm{m} + Nd + d_1$ and the additional covering magnetic layer of YIG of thickness d_m, as shown in Fig. 7. The unit cell of the photonic–magnonic crystal is presented in circular inset of Fig. 7.

5.2.1. *Method*

We assume that electromagnetic waves with the wave vector $\mathbf{k}_\mathrm{EM}$ is incident from vacuum at an angle θ on the right surface of the photonic–magnonic crystal structure depicted in Fig. 7(b) in the plane xy. For the case of in-plane magnetized YIG layers, this mutual orientation of the magnetization vector and $\mathbf{k}_\mathrm{EM}$ corresponds to the longitudinal magneto-optical configuration.[11] In the optical and near infrared (IR) regimes the dispersive refractive indices of TiO_2

and SiO_2, $n_1(\lambda)$ and $n_2(\lambda)$, respectively, have the form presented in Ref. [67].

Both dielectric compounds (the titanate oxide and the silicon oxide, medium 1 and 2, respectively) are characterized by cubic symmetry of their elementary unit cell and the dielectric tensors of these materials have the diagonal forms with dielectric permittivities $\varepsilon_1(\lambda) = n_1^2(\lambda)$ and $\varepsilon_2(\lambda) = n_2^2(\lambda)$, respectively.

For the YIG layers we use the dispersive refractive index within the IR wavelength interval from $1.2\,\mu$m till $5.8\,\mu$m which is well approximated by the formula given in Ref. [68]. In near IR regime YIG possesses bigyrotropic properties and we take into account the off-diagonal components of the dielectric permittivity and magnetic permeability tensors. For the case of magnetization vector $\mathbf{M}$ directed along the y-axis, the tensors of dielectric permittivity and magnetic permeability have the form given in Ref. [11].

$$\hat{\varepsilon}_{\mathrm{m}} = \begin{pmatrix} \varepsilon_{\mathrm{m}} & 0 & i\varepsilon' \\ 0 & \varepsilon_{\mathrm{m}} & 0 \\ -i\varepsilon' & 0 & \varepsilon_{\mathrm{m}} \end{pmatrix}, \quad \hat{\mu}_{\mathrm{m}} = \begin{pmatrix} \mu_{\mathrm{m}} & 0 & i\mu' \\ 0 & \mu_{\mathrm{m}} & 0 \\ -i\mu' & 0 & \mu_{\mathrm{m}} \end{pmatrix}. \tag{39}$$

According to Ref. [69] for YIG the off-diagonal material tensor elements are $\varepsilon' = -2.47 \cdot 10^{-4}$ and $\mu' = 8.76 \cdot 10^{-5}$. For the considered frequency regime $\mu_{\mathrm{m}} = 1$ and $\varepsilon_{\mathrm{m}} = n_{\mathrm{m}}^2(\lambda)$.

For our calculations of transmittivity spectra of the photonic–magnonic crystal the 4D transfer matrix method[70] has been used. The (4×4) total transfer matrix $\hat{T}_{\mathrm{tot}}$ connects the electromagnetic waves' field magnitudes at the right and left surfaces of the the photonic–magnonic crystal as:

$$\hat{T}_{\mathrm{tot}} = \hat{A}_{\mathrm{m}} \hat{E}_{\mathrm{m}}(d_{\mathrm{m}}) (\hat{T})^M \hat{S}_{\mathrm{m}0}, \tag{40}$$

where the transfer matrix $\hat{T}$, corresponding to the period D, is written as:

$$\hat{T} = \hat{S}_{\mathrm{m}1} \hat{E}_1(d_1) (\hat{T}_0)^N \hat{S}_{1\mathrm{m}} \hat{E}_{\mathrm{m}}(d_{\mathrm{m}}) \tag{41}$$

with the subperiod transfer matrix $\hat{T}_0$, corresponding to the period formed with the pair of dielectric layers 1 and 2:

$$\hat{T}_0 = \hat{S}_{12} \hat{E}_2(d_2) \hat{S}_{21} \hat{E}_1(d_1). \tag{42}$$

It should be mentioned that the matrix $\hat{T}_0$ has a block form $\hat{T}_0 = \text{diag}\left[\hat{T}_{0,s}, \hat{T}_{0,p}\right]$ with (2×2) matrices $\hat{T}_{0,\gamma}$, where $\gamma = (s, p)$ corresponds to s- and p-polarized electromagnetic waves.[71]

In Eqs. (40)–(42) the matrices $\hat{S}_{\text{ij}}$ $(i, j = 0, 1, 2, m)$ characterize the transitions of electromagnetic waves through the boundaries of the corresponding media (see details in Refs. [18, 71]). The diagonal matrices $\hat{E}_j(d_j)$, $(j = 1, 2, m)$ present the phase incursions within the corresponding dielectric and magnetic layers.[18]

In the case of the infinite two-periodic magneto-photonic crystals the dispersion relations of the normal electromagnetic waves has the following form[71]:

$$\cos(k_{\pm,\,x}\, D) = \frac{1}{4}\left(\text{Tr}\,(\hat{T}) \pm \sqrt{2\text{Tr}\,(\hat{T}^2) - (\text{Tr}\,(\hat{T}))^2 + 8}\right), \qquad (43)$$

where the transfer matrix $\hat{T}$ given by Eq. (41) and $k_{\pm}$ are the photonic-magnonic crystal's eigenmode wave numbers.[71]

For a dielectric photonic crystal with the period d the normal electromagnetic waves are s- and p-polarized waves with the dispersion relations

$$\cos(k_{x,\gamma}\, d) = \frac{1}{2}\text{Tr}\,(\hat{T}_{0,\gamma}), \quad (\gamma = \text{s, p}) \qquad (44)$$

where $\hat{T}_{0,\gamma}$ are the corresponding parts of the block matrix $\hat{T}_0$, given by Eq. (42) and $k_{x,\gamma}$ are the wave numbers for eigenmodes of photonic crystal. At the normal incidence of light $k_{x,\text{s}} = k_{x,\text{p}}$, and $k_{+,x} = k_{-,x}$.

5.2.2. *Results*

We calculate the dispersion and transmittivity spectra within the wavelength range from $\lambda_{\min} = 0.7\,\mu$m till $\lambda_{\max} = 5.0\,\mu$m where the dielectric materials TiO_2 and SiO_2, forming the composite layer, as well as magnetic YIG are transparent. The number of the periods is chosen to be $M = 9$, while the number of the unit cells in the dielectric photonic crystal layers (subperiods) N is varying under condition, that $d_{\text{d}} = Nd + d_1 = 1.9\,\mu$m is fixed.

We consider the incidence of linear s- or p-polarized electromagnetic waves on the right-side surface of photonic-magnonic crystal

(see Fig. 7 (b)). At the left-side surface of the photonic-magnonic crystal the transmitted elliptically polarized wave is a combination of the electromagnetic wavess of s- and p-polarizations which can be experimentally separated using the polarizing filter.

In the presence of magnetic layers in a photonic structure, the transmittivity matrix has four non-zero components: the diagonal components $T_{\rm ss}$, $T_{\rm pp}$ and off-diagonal ones $T_{\rm sp}$, $T_{\rm ps}$. The diagonal components are responsible for the experimental geometry when the incident s- or p-polarized input light gives the output light of the same polarization (s or p, respectively). The non-zero off-diagonal components $T_{\rm sp}$ and $T_{\rm ps}$ are due to the magnetic layers, and they correspond to the other two experimental geometries: when the s-polarized input light gives p-polarized output and, vice versa, the p-polarized input light produces the s-polarized output.

In Figs. 9(a)–(f) we present the color maps of the logarithm of absolute values of the transmittivities $\log(|T_{\rm ss}|)$ and $\log(|T_{\rm pp}|)$ (the left and right columns, respectively), as functions of frequency of electromagnetic waves and the incidence angle θ for the photonic–magnonic crystal based on the magnetic (YIG) layers and composite dielectric layers $(TiO_2/SiO_2)^N$ containing N dielectric subperiods in the cases of $N = 3$ (Figs. 9(a) and 9(b)), $N = 5$ (Figs. 9(c) and 9(d)), and $N = 7$ (Figs. 9(e) and 9(f)). As $d_{\rm d} = 1.9\,\mu$m is assumed to be the fixed value, the dielectric layer thicknesses d_1 and d_2 depend on N and we obtain $d_1 \approx 0.235\,\mu$m and $d_2 \approx 0.335\,\mu$m for $N = 3$; $d_1 \approx 0.141\,\mu$m, $d_2 \approx 0.211\,\mu$m, for $N = 5$, and $d_1 \approx 0.103\,\mu$m, $d_2 \approx 0.154\,\mu$m, corresponding to the photonic–magnonic crystal with $N = 7$. We concentrate our attention on the lowest in frequency photonic bands within the frequency range from $\omega_{\rm min} = 0.38$ rad·PHz to $\omega_{\rm max} = 2.69$ rad·PHz.

To investigate the influence of magnetic layers on the transmittivity spectra, we compare the photonic band gaps (PBGs) for the photonic–magnonic crystal with those of pure dielectric infinite photonic crystal with the unit cell (TiO_2/SiO_2). In Figs. 9(a)–(f) the dashed lines denote the PBG edges for the infinite dielectric photonic crystals of structure with the layer thicknesses d_1 and d_2, corresponding to those of the photonic-magnonic crystal with

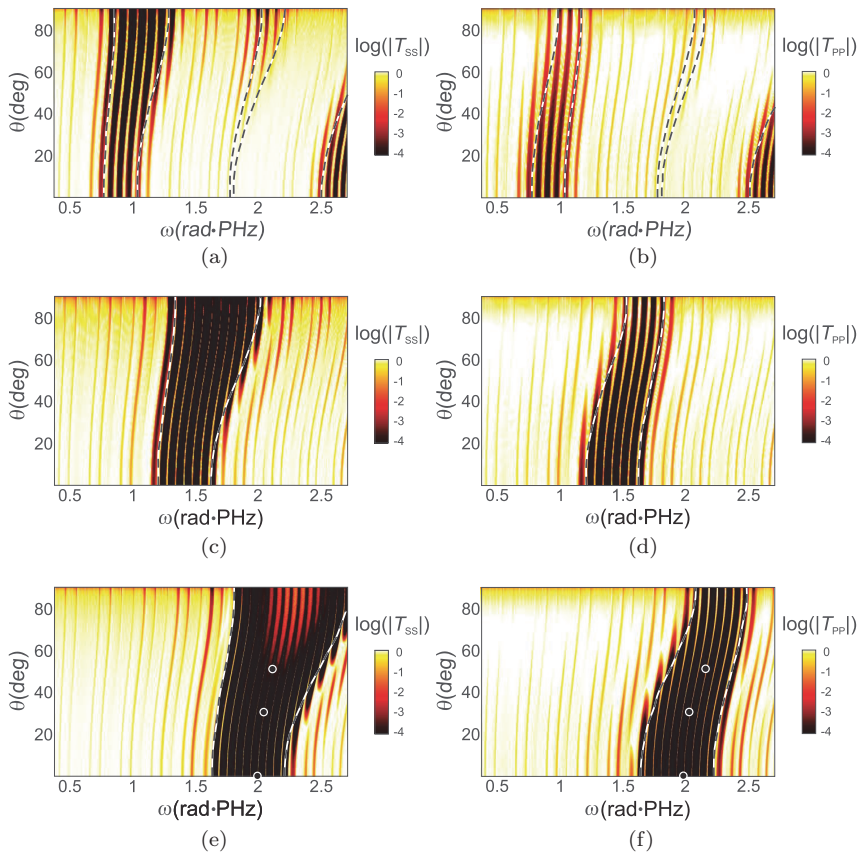

Fig. 9. The electromagnetic waves transmittivity spectra of the photonic–magnonic crystal with N dielectric composite layers $(TiO_2/SiO_2)^N$ and magnetic (YIG) layers as a function of the incidence angle and frequency of electromagnetic waves: (a) and (b) $N = 3$, (c) and (d) $N = 5$, and (e) and (f) $N = 7$.[18] The left and right columns correspond to $\log(|T_{ss}|)$ and $\log(|T_{pp})|$, respectively. The black color marks the photonic band gaps (PBGs) The dotted lines denote the PBG edges for the infinite dielectric photonic crystal with the unit cell (TiO_2/SiO_2). The circles in (e,f) mark the inside-PBG modes which spectra are zoomed in Fig. 10.

N periods. As one can see from Figs. 9(a)–(f), for $N = 3, 5, 7$, the positions of PBGs for pure dielectric photonic crystals and corresponding photonic–magnonic crystals almost coincide, so the PBGs of the infinite dielectric photonic crystal is a little narrower.

Moreover, in the case of $N = 3$ in the spectra of the infinite dielectric photonic crystal the additional PBG band starts to form in vicinity of $\omega \simeq 1.7$ rad·PHz. In the cases of $N = 3$, at normal incidence of light there are four inside-PBG bands, which are presented as bright stripes in Figs. 9(a), and 9(b). The inside-PBG modes are neither equivalent nor equidistant. One can see from Figs. 9(a), and 9(b) that with increasing θ the high frequency PBG edge splits and the new two inside-PBG modes appear. For $N = 3$ when $\theta \approx 65^\circ$, the first inside-PBG mode merges with the low frequency PBG edge and as a result, at large incidence angles only tree inside-PBG modes remain. As one can see from Figs. 9(a)–(f), with increasing of the incidence angle, both PBG edges slightly shift to higher frequency range. At grazing incidence for $|T_{\rm ss}|$ the PBG widths become broader then for normal incidence, while for $|T_{\rm pp}|$ the PBG widths become narrower. The similar peculiarity are present in the spectra in the cases of larger N (see the details in Refs. [18,19]). The number of inside-PBG bands at normal incidence increases to 7 for the photonic–magnonic crystal with $N = 5$ and to 10 for the case of $N = 7$. For all N, for s-polarized light the inside-PBG bands are essentially narrowing with increase of the incidence angle while for p-polarized light the inside-PBG modes broaden with the increase of θ. In all cases of N, the maximal values of transmittivities within all inside-PBG bands is very close to unity. Comparing the corresponding parts of figures: Figs. 9(a) and 9(b), Figs. 9(c) and 9(d), Figs. 9(e) and 9(f), one can see, that the increase of the subperiods number N in the composite dielectric layers leads to essential shift of the PBGs to higher frequencies for both polarizations. In all cases ($N = 3, 5, 7$), the positions of the PBG edges and inside-PBG bands at $\theta = 0$ are the same for $|T_{\rm ss}|$ and $|T_{\rm pp}|$.

In the considered photonic–magnonic crystal in the longitudinal magneto-optical configuration the off-diagonal components $T_{\rm sp}$ and $T_{\rm ps}$ are of the order 10^{-3}. The positions of the PBG edges and inside-PBG modes for $T_{\rm sp}$ and $T_{\rm ps}$ coincide with those for the corresponding diagonal components of the transmittivity matrix ($T_{\rm ss}$ and $T_{\rm pp}$, respectively). Despite the fact that the off-diagonal components of the transmittivity matrix are two orders of magnitude smaller then

the diagonal ones, they play important role in the magneto-optical effects, such as Faraday rotation and Kerr effect.

We also calculated the analogous spectra of electromagnetic waves for the photonic structure, which differs from those, considered above, only by replacing of the dielectric composite layers with the homogeneous dielectric material TiO_2 of the same thickness $d_{\rm d} = 1.9\ \mu$m. For this structure there is no PBGs in the transmittivity spectra for s- and p-polarized electromagnetic waves in the considered frequency range. It means that the PBGs observed in photonic–magnonic crystal with double periodicity are due to the subperiodic structure of the dielectric layers.

To have more insight into physics of the inside-PBG bands in the photonic–magnonic crystals under consideration, we calculate the transmittivity in the vicinity of these inside-PBG bands in a narrow frequency range. It appears, that the inside-PBG band exhibits the fine-structure, i.e., each inside-PBG band consists of a set of subpeaks. In Fig. 10, we show in details one of the inside-PBG band from the PBG for $|T_{\rm ss}|$ spectra and for $|T_{\rm pp}|$ for the photonic–magnonic crystal with the dielectric composite with $N = 7$ subperiods (i.e., the same as was studied in Figs. 9(e), 9(f)) for the cases of normal incidence of light Fig. 10(a), for $\theta = 30^\circ$ Fig. 10(b) and $\theta = 50^\circ$ Fig. 10(c). The inside-PBG band consists of six very narrow and high subpeaks with $|T_{\rm ss}(\omega_{\rm sub})| \approx |T_{\rm pp}(\omega_{\rm sub})| \sim 1$, and the number of fine-structure subpeaks depends on the periods in the magnonic crystal. For the normal incidence the subpeaks for $|T_{\rm ss}|$ and $|T_{\rm pp}|$ spectra coincide, as we previously observed for the PBG edges and inside-PBG bands in the wider frequency ranges.[18] It should be noted that in the case of the infinite photonic-magnonic crystal the fine structure of the inside-PBG peaks disappears as all subpeaks merge.

We also investigated properties of the electromagnetic waves spectra of the photonic–magnonic crystal with magnetic (YIG) layers of thicknesses D_1 and D_2 alternating through the composite structure $(TiO_2/SiO_2)^3TiO_2$.[20] Combination of YIG layers and non-magnetic composite structure thus forms a photonic–magnonic crystal with the supercell period $D = D_1 + D_2 + 2d_{\rm d}$ (see Fig. 11). The number

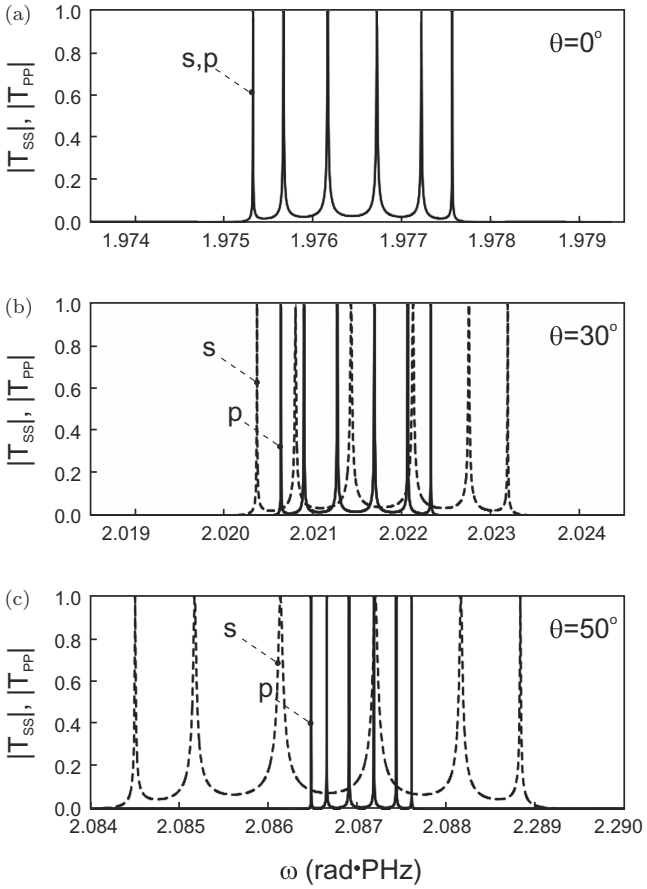

Fig. 10. The exemplary fine-structure of the inside-PBG band for $|T_{\rm ss}|$ and $|T_{\rm pp}|$ transmittivity spectra in photonic–magnonic crystal composed of the $(TiO_2/SiO_2)^7$ multilayers and magnetic (YIG) layers, for normal and oblique electromagnetic wave incidence angles: (a) $\theta = 0$ (normal incidence), (b) $\theta = 30^\circ$, and (c) $\theta = 50^\circ$.[18] The solid and dashed lines corresponds to the s- and p-polarized electromagnetic waves, respectively. In (a) both curves overlap.

of the supercells is fixed to 7. For the numerical calculations, we choose the thicknesses of the dielectric photonic crystals to be equal $d_{\rm d} = 1.9\,\mu$m, with TiO_2 and SiO_2 layers of $d_1 = 0.224\,\mu$m and $d_2 = 0.335\,\mu$m, respectively. We vary the thicknesses of YIG layers, starting with $D_1 = D_2 = D_0 = 7.0\,\mu$m and keeping the total thickness of the supercell fixed as $D = 17.8\,\mu$m. Thus, the thicknesses

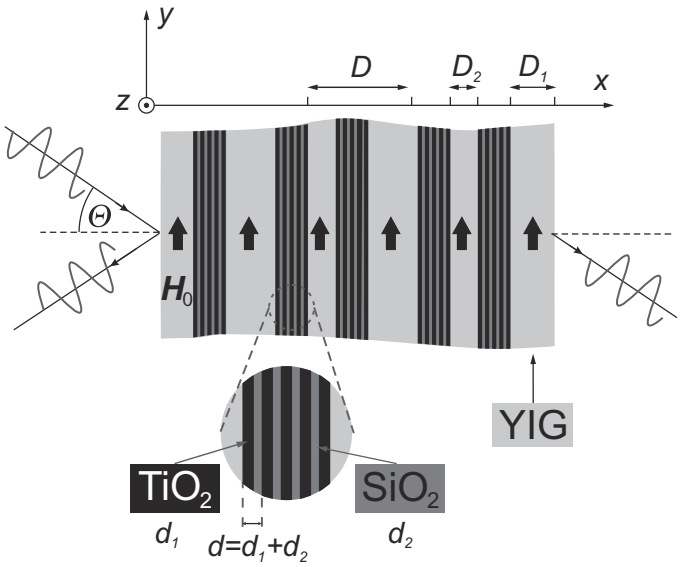

Fig. 11. Schematic of the 1D photonic–magnonic crystal with supercell consisting of two magnetic layers (YIG) of different thicknesses D_1 and D_2 and two insets of dielectric photonic crystal structure $(TiO_2/SiO_2)^3$ TiO_2.

of YIG layers are $D_1 = D_0 \pm \Delta D$ and $D_2 = D_0 \mp \Delta D$, where $\Delta D > 0$ is the deviation of YIG layer thickness from the nominal value D_0. In general, we will consider the photonic–magnonic crystal, where the first YIG layer thickness is decreasing, $D_1 = D_0 - \Delta D$, thus, it is smaller than the thickness of the next YIG layer $D_2 = D_0 + \Delta_D$, which is increasing, i.e., $D_1 < D_2$.

The evolution of the PBG spectrum with reduced deviation of the YIG layer thickness, $\log(T)$ as a function of $\omega d/(2\pi c)$ and $\Delta D/D_0$, is shown in Fig. 12. The transmittivity demonstrates quasi-periodical dependence on $\Delta D/D_0$, with the period of about $0.08D_0$ or $0.56\,\mu$m, which slightly changes with the frequency. The branches of the defect modes of higher and lower intensities alternate in the opposite order for the photonic–magnonic crystals, which begin with thicker and thinner magnetic layers, as one can see comparing the insets in Fig. 12.

In order to explain such dependence of the transmittivity on ΔD, in Figs. 13(a) and 13(b), we plot the transmittivity evolution with

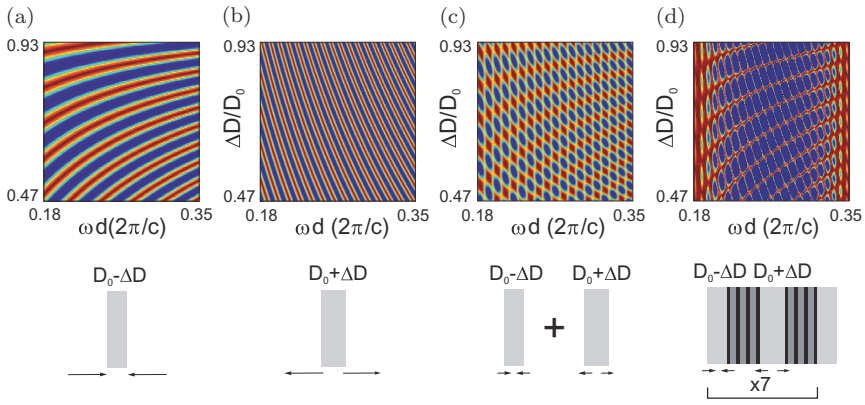

Fig. 12. (a) Evolution of the PBG specter with reduced YIG layer thickness deviation $\Delta D/D_0$ for normal incidence of light. (b) and (c) Four inside-PBG modes in the transmittivity spectra of the photonic–magnonic crystal beginning with (a) thinner ($D_1 < D_2$) and (b) thicker ($D_1 > D_2$) magnetic layers, respectively, within one period.[20] The color shows the value of $\log(T)$.

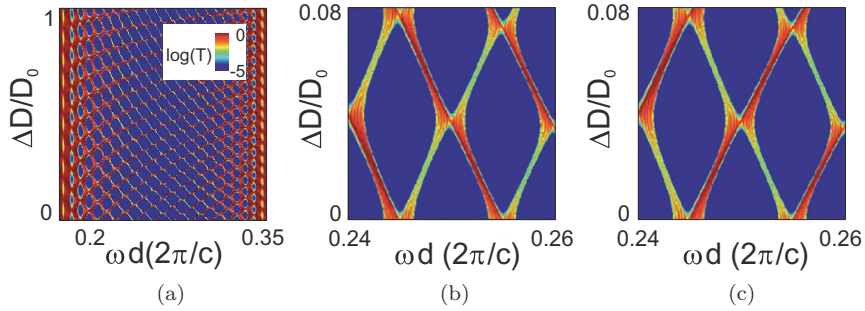

Fig. 13. The transmission of s-polarized light through the single YIG layer as a function of $\Delta D/D_0$ for the normal incidence with (a) decreasing or (b) increasing initial thickness $D_0 = 7.0\,\mu$m and (c) the contributions of increasing and decreasing thicknesses of two YIG layers. (d) The transmission spectrum of the photonic–magnonic crystal with seven superperiods.[20]

$\Delta D/D_0$ for a single magnetic layer with decreasing and increasing thicknesses, respectively. The decrease of YIG layer thickness produces a set of lines going up with increase of frequency. On the contrary, the increase of ΔD gives a set of lines going down with the frequency increase. Combinations of these two contributions,

which take place in the unit supercell and the photonic–magnonic crystal, are illustrated in Figs. 13(c) and 13(d), respectively. Thus, there are two types of the defect modes in the PBG of the photonic–magnonic crystal with two magnetic layers of different thicknesses in the supercell: one of them is caused by increase of one YIG layer thickness in the supercell and another one is due to its decrease. However, from the transmittivity spectrum of the given photonic–magnonic crystal, it is impossible to define, which inside-PBG mode corresponds to increase or decrease of YIG layer thickness.

5.3. *Faraday and Goos–Hänchen effects*

The Faraday effect was discovered in 1845 and defined as the rotation of the polarization plane of a linearly polarized optical beam transmitted through a magnetic material, as schematically shown in Fig. 14(a) in the case of longitudinal magneto-optical configuration.

The Faraday rotation can be used in non-reciprocal devices such as optical isolators and circulators which are used for the routing of optical signals, as well as in the investigation of the magnetic structure of thin magnetic films and magnetic multilayers,[11,72,73] for sensing of magnetic state[74] or even for chemical detection techniques.[75]

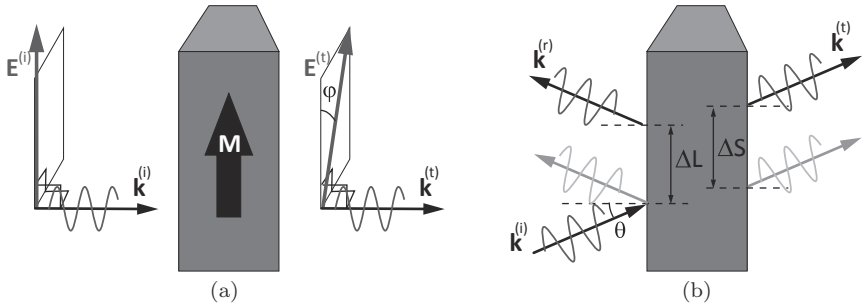

Fig. 14. Schematics of (a) Faraday rotation and (b) Goos–Hänchen effect in photonic structure. Here **E** and **k** are the electric field and wave vector of an electromagnetic wave, θ is incidence angle, φ is Faraday angle, ΔL and ΔS are lateral shifts of the reflected and transmitted beams. The superscripts (i), (r) and (t) refer to the incident, reflected and transmitted waves.

It is convenient to characterize and quantify the magnetically induced polarization changes by using Faraday angles which can be calculated in terms of the transmission matrix elements and defined as

$$\tan(\varphi_{\rm s}) = -{\rm Re}\left(\frac{T_{\rm ps}}{T_{\rm ss}}\right), \quad \tan(\varphi_p) = -{\rm Re}e\left(\frac{T_{\rm sp}}{T_{\rm ss}}\right). \tag{45}$$

It should be noted that reversal of the magnetization of all magnetic layers leads to reversal of both Faraday angles $\varphi_{\rm s}$ and $\varphi_{\rm p}$. Another phenomenon is Goos–Hänchen effect. The lateral shift of a reflected beam relative to its geometrical optics position was reported for the first time in 1947 by Goos and Hänchen in the case of the total internal reflection at the interface between two dielectric media.[76,77] Although this effect was originally predicted and observed at a single interface under the conditions of total internal reflection, similar beam shifts have since been studied in a great variety of configurations and systems, including photonic crystals. Among its many proposed practical applications, the Goos–Hänchen effect has been suggested for instance for the design of chemical sensors,[78–81] biosensors,[82] thermosensors[83] detectors, or detectors of surface roughness.[84]

Figure 14(b) shows schematic of the lateral shift of an electromagnetic beam reflected from (ΔL) and transmitted through (ΔS) a photonic structure. In this chapter, we limit our discussion to the transmission geometry.

Assuming that the incident beam is a Gaussian wavepacket with waist w_0 and using the stationary phase method,[85] one can derive the lateral shift ΔS of each component of the transmitted beam in terms of the complex transmission coefficient T_{ij} and its phase ${\rm Arg}(T_{ij})$, and the x-component of the wave vector k_x as

$$\Delta S_{ij} = -\frac{\partial {\rm Arg}(T_{ij})}{\partial k_x} + \frac{\partial \ln|T_{ij}|}{\partial k_x}\frac{\partial^2 {\rm Arg}\,(T_{ij})}{\partial k_x^2}\left(w_0^2 + \frac{\partial^2 \ln|T_{ij}|}{\partial_x^2}\right)^{-1}. \tag{46}$$

Figs. 15(a) and 15(b) present Faraday angles φ_p of p-polarized and φ_s of s-polarized incident light, respectively, as functions angular

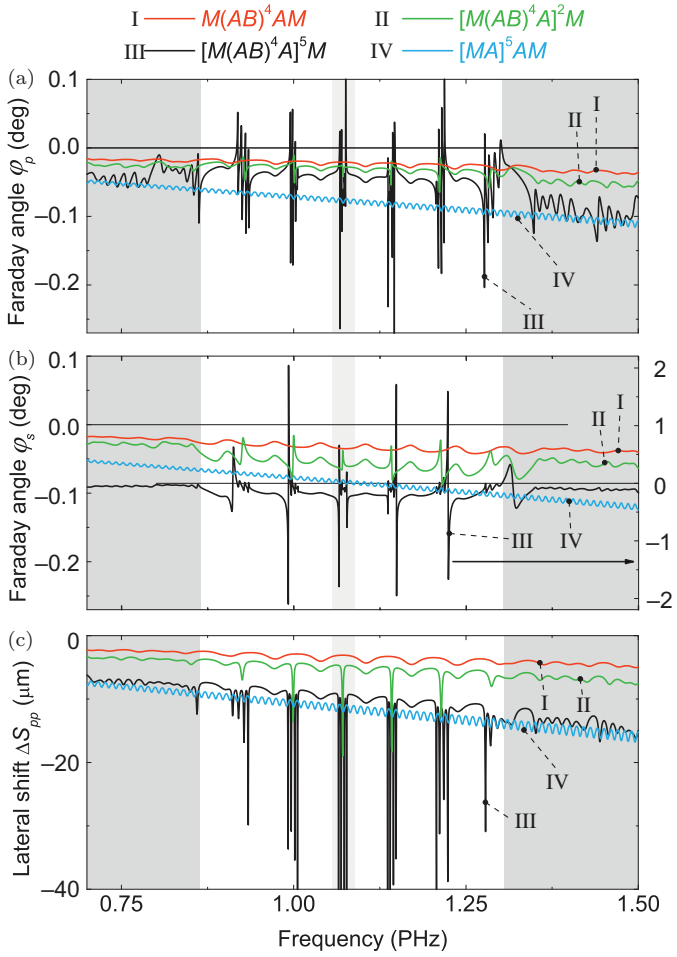

Fig. 15. Spectra of the angles of Faraday rotation φ_{p} (a) and φ_{s} (b), and GHS within the PBG for the incidence angle = 30° and the structures $\mathrm{M(AB)^4AM}$, $\mathrm{[M(AB)^4A]^2M}$, $\mathrm{[M(AB)^4A]^5M}$, and $\mathrm{[MA]^5}$ AM. Note different vertical scale on the left and right vertical axes in (b). The grey areas correspond to the transmission band, and light gray area is zoomed in Fig. 16.

frequency ω for the incidence angle $\theta = 30°$ for the photonic–magnonic crystals with different number K of super-cells.

The Faraday angles in the structure $\mathrm{M(AB)^4AM}$ with four dielectric unit cells and $K = 1$ magnetic super-cell are shown with red lines. In this case, as was mentioned above, the repetition of dielectric

unit cells (AB) between the magnetic layers leads to forming a PBG in the transmittivity spectra of the structure, and narrow-frequency defect modes of high transmittivity appear inside the PBG due to magnetic layers on both sides of the dielectric photonic crystal which act as defect layers. Both Faraday angles φ_{p} and φ_{s} are negative (around 0.02°) and their absolute value slightly increases with increase of ω.

With increase of the number K of the magnetic supercells $\mathrm{M(AB)^4A}$ each inside-PBG mode becomes narrower and splits into set of subpeaks. The Faraday angles inside the PBGs decrease (see green lines for the structures $\mathrm{[M(AB)^4A]^2M}$ with $K = 2$ magnetic super-cell and blue lines for $\mathrm{[M(AB)^4A]^5M}$ with $K = 5$ magnetic super-cell), but in the variations of φ_{s} are larger than those of φ_{p}. Indeed, in the structure $\mathrm{[M(AB)^4A]^5M}$, φ_{s} is about one order of magnitude larger than φ_{p}. Both Faraday angles in the latter case can change sign at some frequencies, and the most noticeable variations of the Faraday angles take place around the inside-PBG modes.

Since Faraday effect increases with thickness of the magnetic layer,[11] it makes sense to compare the Faraday angles in a biperiodic photonic–magnonic crystal $\mathrm{[M(AB)^4A]^5M}$ with Faraday angles in the similar structure with homogeneous dielectric spacer $\mathrm{[MA]^5M}$ with $d_{\mathrm{A}} = d_{\mathrm{d}}$, so that the total thickness of the magnetic layers in these two structures is the same. For the structure with homogeneous dielectric spacer no PBG occurs at the frequency range under consideration for the thicknesses d_{d} and d_{M} which we have chosen for calculations. The Faraday angles are negative (magenta lines); the absolute values of φ_{s} are much less than those in the case of biperiodic photonic–magnonic crystal with $K = 5$ (compare magenta and blue lines in Fig. 15(b) keeping in mind the different vertical scale for these curves). The values of φ_{p}, however, are slightly larger in the case of the structure $\mathrm{[MA]^5M}$ than in the case of $\mathrm{[M(AB)^4A]^5M}$, except the regions which correspond to inside-PBG modes in the latter structure. Thus, periodicity introduced by dielectric photonic crystal modifies drastically the polarization plane rotation and allows achieving larger values of Faraday angles.

In Figs. 16(a) and 16(b) we show the details of a single inside-PBG mode and the corresponding Faraday angles of the light

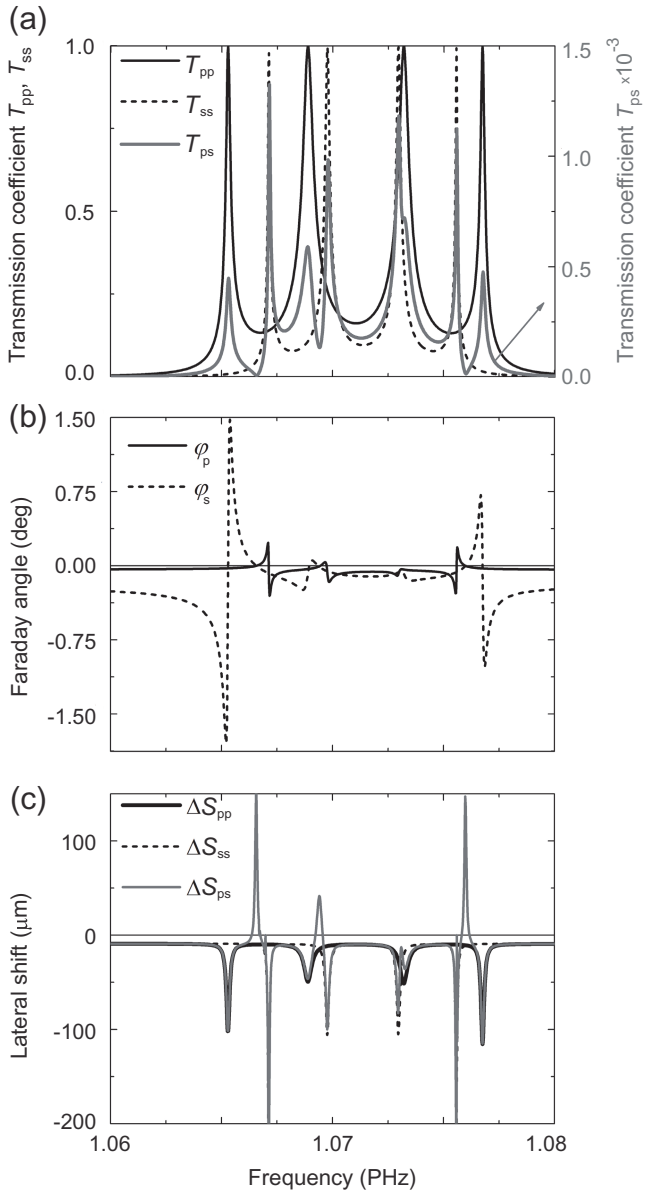

Fig. 16. Fine structure of (a) the inside-PBG mode in the transmission spectra $|T_{\rm pp}|$ (black solid lines), $|T_{\rm ss}|$ (black dashed), $|T_{\rm ps}|$ (gray solid); (b) Faraday rotation angles $\varphi_{\rm p}$ (black solid lines) and $\varphi_{\rm s}$ (black dashed lines); (c) Goos–Hänchen $\Delta S_{\rm pp}$ (black solid lines), $\Delta S_{\rm ss}$ (black dashed lines), and $\Delta S_{\rm sp}$ (gray solid lines) for the incidence angle $\theta = 30^\circ$ and the structure $[{\rm M(AB)^4A}]^5{\rm M}$.[21]

transmitted through a biperiodic photonic–magnonic crystal of the structure $[M(AB)^4A]^5M$. The positions of the Faraday angle maxima do not correspond to position of the inside-PBG mode peaks in the spectra of the diagonal transmission coefficients, as follows from the comparison of black solid and gray solid lines in Figs. 16(a) and 16(b). The origin of this behavior lies in the complex interplay between the diagonal and off-diagonal components of the transmission matrix (the frequency positions of the subpeaks of $T_{\rm pp}$ and $T_{\rm ss}$ spectra are different but overlap with those in $T_{\rm ps}$ spectrum — showed by black dashed line in Fig. 16(a)), whose ratio defines the values of $\varphi_{p,s}$ (see Fig. 14).

It should be noted that when the diagonal transmittivity coefficient $T_{\rm ss}$ is maximal, the Faraday angle reaches values up to 0.1° for s-polarized incident light, whereas for p-polarized incident light the Faraday angle does not exceed -0.02° at the corresponding transmittivity $T_{\rm pp}$ peaks (compare Figs. 16(a) and 16(b)).

Frequency dependence of the lateral shift $\Delta S_{\rm pp}$ is shown in Fig. 15(c) for the incidence angle $\theta = 30^\circ$ for the photonic–magnonic crystal structures with different number K of super-cells. The lateral shift is negative and overall increases with increase of the super-cell number K. The series of abrupt peaks of the lateral shift appear at the frequencies of the inside-PBG modes. In the case when the magnetic layers are separated by homogeneous dielectric layer, the lateral shift is slightly larger (in absolute value) at the frequencies away from the inside-PBG modes than the shift in the similar biperiodic structure. In the latter, at the inside-PBG frequencies, the lateral shift can reach large values about 100λ (see for details Fig. 16(c)).

The lateral shift demonstrates the same fine structure, and the frequency positions of the subpeaks of $\Delta S_{\rm ij}$ coincide with those of T_{ij}, as shown in Figs. 16(a) and 16(c). The lateral shift $\Delta S_{\rm ps}$ of the cross-polarized contribution to the transmitted light can be as negative, as positive (gray line in Fig. 16(c)), contrary to $\Delta S_{\rm pp}$ and $\Delta S_{\rm ss}$ which are always negative. Positions of the positive maxima of $\Delta S_{\rm ps}$ correspond to the position of the gaps between the subpeaks of $T_{\rm ps}$ (compare gray lines in Figs. 16(a) and 16(c)). It should be

noted that not every gap in T_{ps} is accompanied by a positive peak of the lateral shift. For instance, in the middle of the inside-PBG mode (at $\omega \approx 1.072\,\mathrm{rad\ PHz}$) T_{ps} exhibits a smooth change which does not result in large variations of its phase and, according to Eq. (46), does not produce a lateral shift peak. Contrary to the Faraday angles, the positions of the lateral shift peaks of *p*- and *s*-polarized light correspond to those of the transmittivity maxima.

6. Summary

The light can be strongly confined in the magnetic layers placed periodically in the structure of a photonic crystal. This localization is possible for the frequencies in the range of PBGs. Due to the strong localization of inside-PBG modes in magnetic medium, the magneto-optical effects are enhanced. We observed the increase of the Faraday rotation for inside-PBG modes. For the magnetic layers magnetized in-plain, the increase in Faraday rotation is particulate strong for *s*-polarized incoming light. The inside-PBG modes are decaying exponentially when penetrating the sections of photonic crystal but can still weakly interact each other. Therefore, they exhibit fine spectral structure which is the signature of their collective character resulting from the periodic repetitions of magnetic layers.

The considered periodic stack of magnetic layers separated by non-magnetic spacers (i.e., the sections of photonic crystals) forms also the magnonic crystals for spin waves. The spin-wave modes are excited only in magnetic layers but the spin-wave dynamics can be coherent in the whole system due to demagnetizing field penetrating the non-magnetic spacers. So, we can consider the spin-wave propagation in arbitrary direction, including also the propagation between the magnetic layers. For in-plane magnetized and infinitely extended magnetic layers, this coupling mechanism is efficient only for oblique direction of wave vector. In other words, the spin-wave propagation from layer to layer has to accompanied by the component of the spin-wave propagating in-plane.

The discussed structures, called photonic–magnonic crystals support the existence both the electromagnetic waves and spin waves.

We expect that photonic inside-PBG modes, localized in magnetic layers, can couple to spin waves more effectively than other kinds of electromagnetic modes.

Acknowledgments

We acknowledge funding from the EU Horizon 2020 project MagIC No. 644348 and National Science Centre of Poland Grants Nos. UMO-2016/21/B/ST3/00452 and UMO-2017/24/T/ST3/00173. N.N.D. and Y.S.D. acknowledge support from the Russian Foundation for Basic Research (RFBR) under project No. 19-42-730008. Y.S.D. acknowledges support from Conseil Régional de Bretagne, France, under project SPEACS, and from École Nationale d'Ingénieurs de Brest, France, under project HF-CCCP, and I.L.L. acknowledges support from COST under project CA17123 MAGNETOFON. J.R. acknowledges the financial support of the National Science Centre Poland under the decision DEC-2018/30/E/ST3/00267.

References

1. A. Gurevich and G. A. Melkov, *Magnetisation Oscillations and Waves*, CRC, Boca Raton (1996).
2. A. I. Akhiezer, V. G. Bar'yakhtar, and S. V. Peletminskii, *Spin Waves*, Wiley, New York (1968).
3. M. G. Cottam, *Spin Waves in Magnetic Films and Superlattices*, World Scientific, Singapore (1984).
4. D. D. Stancil and A. Prabhakar, *Spin Waves: Theory and Applications*, Springer, New York (2009).
5. J. D. Jackson, *Classical Electrodynamics*, Wiley, New York (1998).
6. V. Kruglyak, S. Demokritov, and D. Grundler, Magnonics, *J. Phys. D: Appl. Phys.* **43**(26), 264001 (2010).
7. A. V. Chumak, A. A. Serga, and B. Hillebrands, Magnonic crystals for data processing, *J. Phys. D: Appl. Phys.* **50**, 244001 (2017). ISSN 1361-6463.
8. S. O. Demokritov, *Spin Wave Confinement*, Jenny Stanford Publishing, Singapure (2009).
9. S. O. Demokritov, *Spin Wave Confinement: Propagating Waves,* 2nd edn., Jenny Stanford Publishing, Singapure (2017).

10. D. J. Lockwood and M. G. Cottam, *Light Scattering in Magnetic Solids*, Wiley, New York (1986).
11. A. K. Zvezdin and V. A. Kotov, *Modern Magnetooptics and Magnetooptical Materials*, Institute of Physics Publishing, Bristol (1997).
12. A. Kirilyuk, A. V. Kimel, and T. Rasing, Ultrafast optical manipulation of magnetic order, *Rev. Mod. Phys.* **82**, 2731 (2010). ISSN 1539-0756.
13. M. Krawczyk and D. Grundler, Review and prospects of magnonic crystals and devices with reprogrammable band structure, *J. Phys.: Cond. Matt.* **26**, 123202 (2014).
14. J. D. Joannopoulos, S. G. Johnson, J. N. Winn, and R. D. Meade, *Photonic Crystals: Molding the Flow of Ligth*, Prinston Univeristy Press, Prinston (1994).
15. M. Inoue, M. Levy, and A. V. Baryshev, *Magnetophotonics: from Theory to Applications*, Springer, Berlin, New York (2013).
16. M. Inoue, R. Fujikawa, A. Baryshev, A. Khanikaev, P. B. Lim, H. Uchida, O. Aktsipetrov, A. Fedyanin, T. Murzina, and A. Granovsky, Magnetophotonic crystals, *J. Phys. D: Appl. Phys.* **39**, R151 (2006). ISSN 1361-6463.
17. I. L. Lyubchanskii, N. N. Dadoenkova, M. I. Lyubchanskii, E. A. Shapovalov, and T. Rasing, Magnetic photonic crystals, *J. Phys. D: Appl. Phys.* **36**(18), R277 (2003). ISSN 1361-6463.
18. J. W. Kłos, M. Krawczyk, Y. S. Dadoenkova, N. N. Dadoenkova, and I. L. Lyubchanskii, Photonic–magnonic crystals: Multifunctional periodic structures for magnonic and photonic applications, *J. Appl. Phys.* **115**, 174311 (2014). ISSN 1089-7550.
19. J. W. Kłos, M. Krawczyk, Y. S. Dadoenkova, N. N. Dadoenkova, and I. L. Lyubchanskii, Spin waves and electromagnetic waves in photonic–magnonic crystals, *IEEE Trans. Magn.* **50**, 1 (2014). ISSN 0018-9464.
20. Y. S. Dadoenkova, N. N. Dadoenkova, I. L. Lyubchanskii, J. W. Kłos, and M. Krawczyk, Confined states in photonic–magnonic crystals with complex unit cell, *J. Appl. Phys.* **120**, 073903 (2016). ISSN 1089-7550.
21. Y. S. Dadoenkova, N. N. Dadoenkova, I. L. Lyubchanskii, J. W. Kłos, and M. Krawczyk, Faraday effect in bi-periodic photonic–magnonic crystals, *IEEE Trans. Magn.* **53**, 1 (2017). ISSN 0018-9464.
22. Y. S. Dadoenkova, N. N. Dadoenkova, J. W. Kłos, M. Krawczyk, and I. L. Lyubchanskii, Goos–Hänchen effect in light transmission through biperiodic photonic–magnonic crystals, *Phys. Rev. A.* **96**, 043804 (2017). ISSN 1094-1622.
23. P. A. Pantazopoulos, N. Stefanou, E. Almpanis, and N. Papanikolaou, Photomagnonic nanocavities for strong light–spin-wave interaction, *Phys. Rev. B.* **96**, 104425 (2017). ISSN 1550-235X.

24. P. A. Pantazopoulos, N. Papanikolaou, and N. Stefanou, Tailoring coupling between light and spin waves with dual photonic–magnonic resonant layered structures, *J. Opt.* **21**, 015603 (2018). ISSN 2040-8986.
25. P. A. Pantazopoulos and N. Stefanou, Layered optomagnonic structures: Time Floquet scattering-matrix approach, *Phys. Rev. B.* **99**, 144415 (2019). ISSN 1550-235X.
26. L. Landau and E. Lifshitz. On the theory of the dispersion of magnetic permeability in ferromagnetic bodies. In L. Pitaevski, (ed.), *Perspectives in Theoretical Physics*, Pergamon, Amsterdam (1992), pp. 51–65.
27. M. Lakshmanan, The fascinating world of the Landau–Lifshitz–Gilbert equation: An overview, *Philos. Trans. Royal Soc. A.* **369**, 1280 (2011).
28. T. L. Gilbert, A phenomenological theory of damping in ferromagnetic materials, *IEEE Trans. Magn.* **40**, 3443 (2004). ISSN 0018-9464.
29. W. Heisenberg, Zur Theorie des Ferromagnetismus, *Z. Phys.* **49** (9), 619 (1928). ISSN 0044-3328.
30. N. Ashcroft and N. Mermin, *Solid State Physics*, Holt, Rhinehart and Winston, Philadelphia (1976).
31. M. Krawczyk, M. L. Sokolovskyy, J. Kłos, and S. Mamica, On the formulation of the exchange field in the Landau–Lifshitz equation for spin-wave calculation in magnonic crystals, *Advances in Condensed Matter Physics.* **2012**, 764783 (2012).
32. A. Aharoni, Magnetostatic energy calculations, *IEEE Trans. Magn.* **27** (4), 3539 (1991). ISSN 0018-9464.
33. J. A. Osborn, Demagnetizing factors of the general ellipsoid, *Phys. Rev.* **67**, 351 (1945). ISSN 1536-6065.
34. R. I. Joseph and E. Schlmann, Demagnetizing field in nonellipsoidal bodies, *J. Appl. Phys.* **36**, 1579 (1965). ISSN 1089-7550.
35. F. Bloch, *Zur Theorie des Ferromagnetismus, Z. Phys.* **61**, 206 (1930). ISSN 0044-3328.
36. T. Holstein and H. Primakoff, Field dependence of the intrinsic domain magnetization of a ferromagnet, *Phys. Rev.* **58**, 1098 (1940). ISSN 1536-6065.
37. G. Heller and H. A. Kramer, *Ein klassisches Modell des Ferromagnetikums und seine nachtrgliche Quantisierung im Gebiete tiefer Temperaturen, Proc. K. Akad. Wet.* **37**, 378 (1934).
38. L. R. Walker, Resonant modes of ferromagnetic spheroids, *J. Appl. Phys.* **29**, 318 (1958). ISSN 1089-7550.
39. J. R. E. R. W. Damon, Magnetostatic modes of a ferromagnet slab, *J. Phys Chem. Solids.* **19**, 308 (1961). ISSN 0022-3697.
40. C. Kittel, On the theory of ferromagnetic resonance absorption, *Phys. Rev.* **73**, 155 (1948).

41. P. C. Fletcher and R. O. Bell, Ferrimagnetic resonance modes in spheres, *J. Appl. Phys.* **30**, 687 (1959). ISSN 1089-7550.
42. C. Thiessen, A simple method for determining magnetostatic mode frequency and pattern, *J. Appl. Phys.* **39**(6), 2875 (1968). ISSN 1089-7550.
43. B. A. Kalinikos, Spectrum and linear excitation of spin waves in ferromagnetic films, *Sov. Phys. J.* **24**, 718 (1981). ISSN 0038-5697.
44. B. A. Kalinikos and A. N. Slavin, Theory of dipole-exchange spin wave spectrum for ferromagnetic films with mixed exchange boundary conditions, *J. Phys. C: Solid State Phys.* **19** (35), 7013 (1986). ISSN 0022-3719.
45. E. Yablonovitch, Inhibited spontaneous emission in solid-state physics and electronics, *Phys. Rev. Lett.* **58**, 2059 (1987). ISSN 1079-7114.
46. S. John, Strong localization of photons in certain disordered dielectric superlattices, *Phys. Rev Lett.* **58**, 2486 (1987). ISSN 1079-7114.
47. C. Sykes, J. Adam, and J. Collins, Magnetostatic wave propagation in a periodic structure, *Appl. Phys. Lett.* **29**, 388 (1976). ISSN 1077-3118.
48. J. P. Parekh and H. S. Tuan, Magnetostatic surface wave reflectivity of a shallow groove on a yig film, *Appl. Phys. Lett.* **30**, 667 (1977). ISSN 1077-3118.
49. J. O. Vasseur, L. Dobrzynski, B. Djafari-Rouhani, and H. Puszkarski, Magnon band structure of periodic composites, *Phys. Rev. B.* **54**, 1043 (1996). ISSN 1550-235X.
50. M. Krawczyk and H. Puszkarski, Magnonic spectra of ferromagnetic composites versus magnetization contrast, *Acta Phys. Polon. A.* **93**, 805 (1998).ISSN 0587-4246.
51. Y. V. Gulyaev and A. A. Nikitov, Magnonic crystals and spin waves in periodic structures, *Doklady Phys.* **46** (10), 687–689 (2001). ISSN 1562-6903.
52. G. Gubbiotti, S. Tacchi, M. Madami, G. Carlotti, A. Adeyeye, and M. Kostylev, Brillouin light scattering studies of planar metallic magnonic crystals, *J. Phys. D: Appl. Phys.* **43** (26), 264003 (2010). ISSN 1361-6463.
53. S. Tacchi, G. Gubbiotti, M. Madami, and G. Carlotti, Brillouin light scattering studies of 2D magnonic crystals, *J. Phys.: Condens. Matter.* **29** (7), 073001 (2017). ISSN 1361-648X.
54. Z. K. Wang, V. L. Zhang, H. S. Lim, S. C. Ng, M. H. Kuok, S. Jain, and A. O. Adeyeye, Observation of frequency band gaps in a one-dimensional nanostructured magnonic crystal, *Appl. Phys. Lett.* **94**, 083112 (2009). ISSN 1077-3118.
55. G. Gubbiotti, S. Tacchi, M. Madami, G. Carlotti, S. Jain, A. O. Adeyeye, and M. P. Kostylev, Collective spin waves in a bicomponent

two-dimensional magnonic crystal, *Appl. Phys. Lett.* **100**, 162407 (2012). ISSN 1077-3118.
56. J. W. Kłos, M. L. Sokolovskyy, S. Mamica, and M. Krawczyk, The impact of the lattice symmetry and the inclusion shape on the spectrum of 2D magnonic crystals, *J. Appl. Phys.* **111**, 123910 (2012). ISSN 1089-7550.
57. J. Rychły, J. Kłos, and M. Krawczyk, Spin wave damping in periodic and quasiperiodic magnonic structures, *J. Phys. D: Appl. Phys.* **49** (17), 175001 (2016). ISSN 1361-6463.
58. M. Zelent, N. Tahir, R. Gieniusz, J. W. Kłos, T. Wojciechowski, U. Guzowska, A. Maziewski, J. Ding, A. O. Adeyeye, and M. Krawczyk, Geometrical complexity of the antidots unit cell effect on the spin wave excitations spectra, *J. Phys. D: Appl. Phys.* **50**, 185003 (2017). ISSN 1361-6463.
59. S. Pan, J. W. Kłos, S. Mieszczak, A. Barman, and M. Krawczyk, Spin waves in periodic antidot waveguide of complex base, *J. Phys. D: Appl. Phys.* **50**, 275003 (2017). ISSN 1361-6463.
60. P. Malago, L. Giovannini, R. Zivieri, P. Gruszecki, and M. Krawczyk, Spin-wave dynamics in permalloy/cobalt magnonic crystals in the presence of a nonmagnetic spacer, *Phys. Rev. B.* **92** (6), 064416 (2015).
61. C. Banerjee, P. Gruszecki, J. W. Kłos, O. Hellwig, M. Krawczyk, and A. Barman, Magnonic band structure in a Co/Pd stripe domain system investigated by Brillouin light scattering and micromagnetic simulations, *Phys. Rev. B.* **96**, 024421 (2017). ISSN 1550-235X.
62. G. Floquet, Sur les équations différentielles linéaires à coefficients périodiques, *Ann. Sci. Ec. Norm. Super.* **12**, 47 (1883). ISSN 0012-9593.
63. F. Bloch, *Uber die Quantenmechanik der Elektronen in Kristallgittern*, *Z. Phys.* **52**, 555 (1929). ISSN 0044-3328.
64. J. Rychły and J. W. Kłos, Spin wave surface states in 1D planar magnonic crystals, *J.Phys. D: Appl. Phys.* **50** (16), 164004 (2017). ISSN 1361-6463.
65. J. Rychły, P. Gruszecki, M. Mruczkiewicz, J. W. Kłos, S. Mamica, and M. Krawczyk, Magnonic crystals prospective structures for shaping spin waves in nanoscale, *Low Temp. Phys.* **41**, 745 (2015). ISSN 1529-7845.
66. M. Mruczkiewicz, M. Krawczyk, V. Sakharov, Y. V. Khivintsev, Y. A. Filimonov, and S. Nikitov, Standing spin waves in magnonic crystals, *J. Appl. Phys.* **113** (9), 093908 (2013). ISSN 1089-7550.
67. E. D. Palik, *Handbook of Optical Constants in Solids*, Academic Press, New York (1991).

68. K.-H. Hellewege, *Landolt-Brnstein: Numerical Data and Functional Relationships in Science and Technology. New Series. Group III: Crystal and Solid State Physics, Vol. 12: Magnetic and Another Properties of Oxides and Related Compounds, Pt. A Garnets and Perovskites*, Springer, Berlin (1978).
69. M. Torfet and H. Le Gall, Theoretical analysis of hybrid modes of magnetooptical waveguides, *Phys. Status Solidi (a).* **63**, 247 (1981). ISSN 1862-6319.
70. D. W. Berreman, Optics in stratified and anisotropic media: 44-matrix formulation, *J. Opt. Soc. Am.* **62**, 502 (1972). ISSN 0030-3941.
71. S. B. Borisov, N. N. Dadoenkova, and I. L. Lyubchanskii, Normal electromagnetic-waves in bigyrotropic magnetooptical layered structure, *Opt. and Spectrosc.* **74** (6), 670–675 (1993). ISSN 0030-400X.
72. M. Mansuripur, *The Physical Principles of Magneto-Optical Recording*, Cambridge University Press, Cambridge (1995).
73. J. Gräfe, M. Schmidt, P. Audehm, G. Schutz, and E. Goering, Application of magneto-optical Kerr effect to first-order reversal curve measurements, *Rev. Sci. Instrum.* **85**, 023901 (2014). ISSN 1089-7623.
74. M. Atature, J. Dreiser, A. Badolato, and A. Imamoglu, Observation of Faraday rotation from a single confined spin, *Nat. Phys.* **3**, 101 (2007). ISSN 1745-2481.
75. N. Dissanayake, M. Levy, A. Chakravarty, P. A. Heiden, N. Chen, and J. V. Fratello, Magneto-photonic crystal optical sensors with sensitive covers, *J. Appl. Phys.* **99**, 091112 (2011). ISSN 1089-7550.
76. F. Goos and H. Hanchen, Ein neuer und fundamentaler Versuch zur Totalreflexion, *Ann. Phys. (Berl.).* **436**, 333–346 (1947). ISSN 1521-3889.
77. F. Goos and H. Lindberg-Hanchen, Neumessung des Strahlversetzungseffektes bei Totalreflexion, *Ann. Phys. (Berl.).* **440**, 251–252 (1949). ISSN 1521-3889.
78. Y. Nie, Y. Li, Z. Wu, X. Wang, W. Yuan, and M. Sang, High-sensitivity temperature sensor using the ultrahigh order mode-enhanced Goos–Hänchen effect, *Opt. Express.* **21**, 13380 (2013). ISSN 1094-4087.
79. J. Sun, X. Wang, C. Yin, P. Xiao, H. Li, and Z. Cao, Optical transduction of E. Coli O157:H7 concentration by using the enhanced Goos-Hänchen shift, *J. Appl. Phys.* **112**, 083104 (2012). ISSN 1089-7550.
80. Y. S. Dadoenkova, F. F. L. Bentivegna, V. V. Svetukhin, A. V. Zhukov, R. V. Petrov, and M. I. Bichurin, Controlling optical beam shifts upon reflection from a magneto-electric liquid-crystal-based system for applications to chemical vapor sensing, *Appl. Phys. B* **123**, 107 (2017). ISSN 1432-0649.

81. Y. S. Dadoenkova, F. F. L. Bentivegna, and M. I. Bichurin, Principle of tunable chemical vapor detection exploiting the angular Goos–Hänchen shift in a magneto-electric liquid-crystal-based system, *J. Opt.* **19**, 095802 (2017). ISSN 2040-8986.
82. T. Tang, C. Li, L. Luo, Y. Zhang, and J. Li, Goos–Hänchen effect in semiconductor metamaterial waveguide and its application as a biosensor, *Appl. Phys. B.* **122**, 167 (2016). ISSN 1432-0649.
83. Y. S. Dadoenkova, F. F. L. Bentivegna, R. V. Petrov, and M. I. Bichurin, Thermal dependence of the lateral shift of a light beam reflected from a liquid crystal cell deposited on a magnetic film, *J. Appl. Phys.* **123**, 033105 (2018). ISSN 1089-7550.
84. Z. Tahmasebi and M. Amiri, Thermal dependence of the lateral shift of a light beam reflected from a liquid crystal cell deposited on a magnetic film, *Phys. Rev. A*. **93**, 4382 (2016). ISSN 1094-1622.
85. K. Artmann, *Berechnung der Seitenversetzung des totalreflektierten Strahles, Ann. Phys. (Berl.)*. **437**, 87–102 (1948). ISSN 1521-3889.